


Floquet Quantum Simulation with Superconducting Qubits

Oleksandr Kyriienko and Anders S. Sørensen

The Niels Bohr Institute, University of Copenhagen, Blegdamsvej 17, DK-2100 Copenhagen, Denmark

 (Received 15 March 2017; revised manuscript received 9 January 2018; published 19 June 2018)

We propose a quantum algorithm for simulating spin models based on the periodic modulation of transmon qubits. Using the Floquet theory, we derive an effective time-averaged Hamiltonian, which is of the general XYZ class, different from the isotropic XY Hamiltonian typically realized by the physical setup. As an example, we provide a simple recipe to construct a transverse Ising Hamiltonian in the Floquet basis. For a 1D system, we demonstrate numerically the dynamical simulation of the transverse Ising Hamiltonian and quantum annealing to its ground state. We benchmark the Floquet approach with a digital simulation procedure and demonstrate that it is advantageous for limited resources and finite anharmonicity of the transmons. The described protocol represents a hardware-efficient quantum software and can serve as a simple yet reliable path towards configurable quantum simulators with currently existing superconducting chips.

DOI: [10.1103/PhysRevApplied.9.064029](https://doi.org/10.1103/PhysRevApplied.9.064029)

I. INTRODUCTION

Quantum simulation relies on exploiting a controllable quantum system to imitate a complex quantum system of interest [1]. It provides an efficient way to solve classically inaccessible problems of material science [2] and quantum chemistry [3,4]. Ultimately, quantum simulation may give access to properties of complex quantum systems with exponential speedup as compared to classical algorithms [5,6]. Superconducting circuits (SCs) [7,8] have recently emerged as one of the prime candidates for realizing full-scale quantum computers, with operations close to the fault-tolerant threshold [9–15]. From the simulation point of view, various protocols were proposed and realized experimentally [16], including the simulation of spin systems [17–19], fermionic models [20], quantum chemistry [21], thermalization [22], synthetic magnetic fields [23], ultrastrong coupling [24,25], and gauge field theories [26]. To demonstrate the full potential of a quantum simulation with SCs, however, there is a need for protocols which can outperform classical protocols for realistic near-term medium-size systems.

Typically, protocols for quantum simulation can be divided into digital and analog (or emulator) types. While these techniques are similar, they exploit different methods to achieve a quantum speedup. The digital approach relies on discretizing the Hamiltonian evolution using a set of quantum gates. A protocol for simulating an arbitrary unitary $\hat{U}(t) = \exp(-i\hat{H}t)$ governed by a Hamiltonian \hat{H} not available in the physical setup exploits the sequential implementation of the available unitaries \hat{U}_ℓ represented by gates. The corresponding unitary of a single digital step j of duration δt can be constructed as

$\hat{U}_j(\delta t) = \prod_\ell \hat{U}_\ell$. This string of unitaries can be recast in terms of Hamiltonians $\hat{U}_j(\delta t) = \prod_m e^{-i\hat{H}_m \delta t}$. An implementation of $N_{\text{Tr}} \rightarrow \infty$ of these Trotter steps combines into a unitary $\hat{U}(t) = \lim_{N_{\text{Tr}} \rightarrow \infty} \hat{U}_j(\delta t)^{N_{\text{Tr}}} \approx e^{-i\hat{H}t}$, where $\hat{H} = \sum_m \hat{H}_m$ and $t = \delta t N_{\text{Tr}}$ [5]. Given a universal set of gates, any required Hamiltonian can, in principle, be simulated. This poses the challenge of implementing long sequences of quantum gates for successful simulation, leading to errors if they have limited fidelity. The digital approach is widely used for quantum simulation with SCs [17–21,24,25], as it is tunable and does not require changing the sample layout to simulate different models.

Analog quantum simulation relies on the actual physical implementation of the required Hamiltonian, corresponding to the emulation of a targeted real system. This is realized on various platforms, including cold atoms in optical lattices [27,28] and trapped ions [29–31]. By exploiting continuous time dynamics, Trotterization errors are minimized, and analog protocols can therefore have superior simulation fidelities. However, they are restricted to the types of Hamiltonian physically realizable in the system. In particular, this is the case for SC quantum systems. Current highly coherent chains of transmons, sketched in Fig. 1, are typically limited to the nearest-neighbor flip-flop type of interqubit interaction provided by the capacitive coupling between them. Thus, they are confined to simulate an isotropic XY -type spin-1/2 model [32]. The accessible models can be enriched by implementing different connections between the qubits to engineer various nonlinear couplings [33–35], engineered interaction through a common bus resonator [36,37], or allowing for the modulation of interqubit interactions to break the

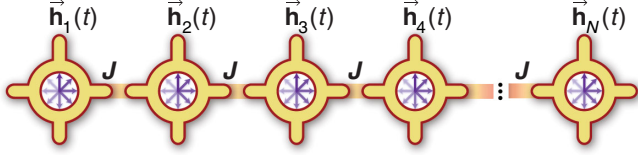


FIG. 1. *Sketch of the system.* A chain of superconducting transmon-type qubits coupled through isotropic XY coupling J . Each qubit is subject to a periodically modulated effective magnetic field $\mathbf{h}_j(t)$.

rotating-wave approximation [38–40]. However, this adds extra complications to experiments and potentially introduces additional errors.

Here, we propose an alternative analoglike simulation strategy, which can be performed without modifications of the system. It is based on using a Floquet basis to perform quantum simulation with superconducting circuits and can be extended to ground-state preparation via quantum annealing. The idea relies on the time-dependent modulation of the Hamiltonian $\hat{\mathcal{H}}(t) = \hat{\mathcal{H}}_0 + \hat{\mathcal{H}}_1(t)$, where $\hat{\mathcal{H}}_0$ is a time-independent part and $\hat{\mathcal{H}}_1(t) = \hat{\mathcal{H}}_1(t+T)$ is harmonically varying with a period $T = 2\pi/\omega$. The corresponding unitary operator for a single period can be rewritten as an effective evolution with a time-independent Hamiltonian given by the Magnus expansion [41,42]. When the frequency of modulation ω is much bigger than the coupling in the static Hamiltonian, $\omega/\|\hat{\mathcal{H}}_0\| \gg 1$, the dynamics of the system can be conveniently represented in terms of a period-averaged Floquet Hamiltonian:

$$\hat{\mathcal{H}}_F = \frac{1}{T} \int_0^T \hat{\mathcal{H}}'_0(t) dt, \quad (1)$$

where $\hat{\mathcal{H}}'_0(t)$ denotes the static Hamiltonian $\hat{\mathcal{H}}_0$ rewritten in the interaction picture with respect to the oscillating part. The resulting Hamiltonian $\hat{\mathcal{H}}_F$ may possess qualitatively different behavior compared to $\hat{\mathcal{H}}_0$. Such a Floquet type of simulation recently gained attention in the cold atom [43] and condensed matter physics communities [44,45], and for SCs was used to study the quasienergies of a single qubit [46]. Here we show how to use similar techniques as a general protocol for a quantum simulation.

We consider qubits with isotropic XY coupling and show that by exploiting fast driving of each site we can tailor the effective Hamiltonian of the system. For concreteness, we focus on one-dimensional chains, but the method can easily be extended to more dimensions or to nonlocal models using a quantum bus. First, we describe how the approach can be used to simulate the dynamics of the transverse Ising model, showing that, as compared to digital protocols, a higher fidelity can be attained. Next, we simulate quantum annealing to the ground state of the transverse Ising model and find that the Floquet approach outperforms the digital for restricted resources, when limited by the

finite anharmonicity of the transmons. Finally, we describe an algorithm for simulating the spin-1/2 XYZ model with the Floquet approach.

II. MODEL

As a physical realization, we consider a capacitively coupled chain of transmon-type qubits (Fig. 1) [11,47–49], where periodically oscillating effective magnetic fields are applied at chosen lattice sites. The time-independent Hamiltonian in the rotating frame $\hat{\mathcal{H}}_0$ contains a nearest-neighbor flip-flop interaction with bare coupling J , corresponding to the isotropic XY spin-1/2 model:

$$\hat{\mathcal{H}}_0 = \sum_{j=1}^{N-1} J(\sigma_j^x \sigma_{j+1}^x + \sigma_j^y \sigma_{j+1}^y). \quad (2)$$

Here σ_j^α ($\alpha = x, y, z$) are spin-1/2 Pauli operators at lattice site j , N denotes the number of qubits in the chain, and we consider open boundary conditions. The time-dependent Hamiltonian $\hat{\mathcal{H}}_1(t)$ contains a periodic magnetic field $\mathbf{h}_j(t)$ which rapidly oscillates along arbitrary axes, and we assume that it differs between even and odd sites:

$$\hat{\mathcal{H}}_1(t) = \sum_{j=1}^{\lfloor N/2 \rfloor} \mathbf{h}_{\text{odd}}(t) \cdot \boldsymbol{\sigma}_{2j-1} + \sum_{j=1}^{\lfloor N/2 \rfloor} \mathbf{h}_{\text{even}}(t) \cdot \boldsymbol{\sigma}_{2j}, \quad (3)$$

where $\lfloor x \rfloor$ and $\lceil x \rceil$ denote floor and ceiling functions, respectively. We assume that the magnetic field is sharply turned on at time $t = 0$ and, thus, explicitly account for the kick operator contribution [43]. Going to the rotating frame with respect to $\hat{\mathcal{H}}_1$ and integrating over a period as in Eq. (1), we get the reduced Floquet Hamiltonian in the general form [Appendix A]

$$\hat{\mathcal{H}}_F = \sum_{\alpha, \alpha' = x, y, z} \sum_{j=1}^{\lfloor N/2 \rfloor} \overline{\xi_{\alpha\alpha'}} \sigma_{2j}^\alpha (\sigma_{2j-1}^{\alpha'} + \sigma_{2j+1}^{\alpha'}), \quad (4)$$

where the time-averaged coefficients $\overline{\xi_{\alpha\alpha'}}$ are defined in Appendix A and are controlled by the effective magnetic fields.

III. RESULTS

A. Transverse Ising model: Dynamics

We first consider the Floquet simulation of the transverse Ising model, which represents a particular case of the more general Floquet Hamiltonian (4).

The intuitive way to describe the realization of the Ising model ($\propto \sigma_1^x \sigma_2^x$) from the isotropic XY case (with interaction type $\propto \sigma_1^x \sigma_2^x + \sigma_1^y \sigma_2^y$) is to take two spins and imagine one to be rotating in a magnetic field. Starting from the flip-flop interaction, if we choose the axis of the magnetic field to be in the \mathbf{e}^x direction, nothing will happen to the first interaction term. At the same time, the rotation of the

second spin leads to oscillations of the second term between $\pm\sigma_1^y\sigma_2^y$ and also induces a $\propto\sigma_1^y\sigma_2^z$ interaction component. For large frequencies of oscillation and a carefully chosen drive amplitude, the plus and minus components will cancel each other, as well as the cross-interaction components, ultimately leaving the Ising term $\propto\sigma_1^x\sigma_2^x$ only.

The transverse Ising model can be realized with a drive of the form $\mathbf{h}_{\text{even}}(t) = (\lambda/2)\omega \cos(\omega t)\mathbf{e}^x + 2h^z(1 + \mathcal{J}_0[2\lambda])^{-1} \cos(\lambda \sin[\omega t])\mathbf{e}^z$ and $\mathbf{h}_{\text{odd}}(t) = h^z\mathbf{e}^z$, where λ is a drive parameter and $\mathcal{J}_0[x]$ denotes the zeroth-order Bessel function of the first kind. The z -directed terms additionally introduce an effective transverse magnetic field h^z . In the infinite frequency limit $|J|/\omega \rightarrow 0$ and for $\lambda = 2.40483$ ($\mathcal{J}_0[\lambda] = 0$), this leads to an effective Hamiltonian of the form [Appendix B]

$$\hat{\mathcal{H}}_F = J_{\text{sim}} \sum_{j=1}^{N-1} \sigma_j^x \sigma_{j+1}^x + h^z \sum_{j=1}^N \sigma_j^z \equiv \hat{\mathcal{H}}_{\text{tIsing}}, \quad (5)$$

where for later reference $J_{\text{sim}} = J$ describes the effective simulated coupling of the model. The ratio between the effective magnetic field in the Floquet basis and the Ising interaction, h^z/J_{sim} , can be controlled by the drive parameters.

We numerically calculate the full dynamics of the system with time-periodic driving of frequency $\omega/|J| = 50$ and access the Floquet dynamics by looking at stroboscopic times nT , where n is an integer [Fig. 2(a)]. The results are compared to an ideal simulation of the transverse Ising Hamiltonian (5), with the initial state $|\psi_{\text{in}}\rangle = \bigotimes_{j=1}^{N/2} (|\uparrow\rangle_{2j-1} - i|\downarrow\rangle_{2j-1})/\sqrt{2} \otimes |\uparrow\rangle_{2j}$. We benchmark the Floquet simulation with a digital protocol [see Appendix C for details and the gate sequence]. It uses the isotropic XY interaction and its rotated version and

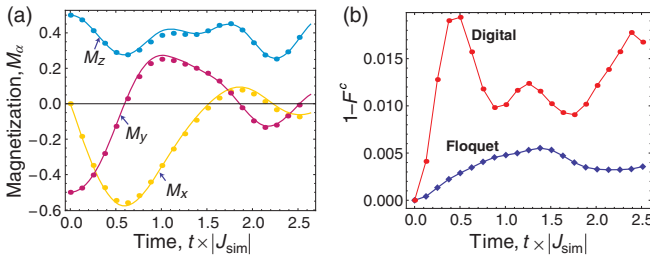


FIG. 2. *Transverse Ising dynamics.* (a) Total normalized magnetization of the $N = 4$ chain $M_\alpha(t) = \langle \psi(t) | \sum_j^N \sigma_j^\alpha | \psi(t) \rangle / N$. Solid curves show the ideal continuous evolution under the transverse Ising Hamiltonian. Bullets correspond to stroboscopic periods of the Floquet dynamics. We set $J < 0$, $h^z/J = 3/2$, and $\omega/|J| = 50$ and run the simulation for a total of 20 stroboscopic periods. (b) Simulation infidelities. Blue diamonds identify the dynamical overlap of the Floquet evolution with the ideal transverse Ising evolution. The red bullets correspond to digital evolution with $N_{\text{Tr}} = 20$ Trotter steps.

approaches the Ising model in the limit of a large number of Trotter periods N_{Tr} [17]. The results in Fig. 2(b) show that the Floquet simulation has a high fidelity $F^c = |\langle \psi_{\text{tIsing}}(nT) | \psi(nT) \rangle|^2$ with exact continuous dynamics at a short time but deviates at later stages due to the finite Floquet frequency. The digital approach shows substantial deviations for this limited N_{Tr} even at short times but will have a rapid convergence with more Trotter steps (see below). We note that a comparison of the number of Floquet periods and Trotter steps may not be a fair comparison, since the latter involves multiple gates.

B. Transverse Ising model: Ground-state preparation

We now study ground-state preparation of the simulated model. To access the ground state, we perform quantum annealing [50], which also serves as a basis for adiabatic quantum computing [51] and may solve NP-complete problems [52]. Using the Floquet basis, we design the Hamiltonian $\hat{\mathcal{H}}_F(t) = J_{\text{sim}} \sum_{j=1}^{N-1} \sigma_j^x \sigma_{j+1}^x + (1 - t/t_f)h^z \sum_{j=1}^N \sigma_j^z$, where the effective magnetic field is linearly turned off during the annealing time t_f . We consider $J_{\text{sim}} < 0$, which allows us to access the ground state of the ferromagnetic x -Ising Hamiltonian. The ideal target state is a maximally entangled state $|\psi_T\rangle = (|+\rangle^{\otimes N} + |-\rangle^{\otimes N})/\sqrt{2}$, where $|\pm\rangle = (|\downarrow\rangle \pm |\uparrow\rangle)/\sqrt{2}$, and we start from the trivial initial state $|\psi_{\text{in}}\rangle = |\downarrow\rangle^{\otimes N}$.

The results of the annealing procedure are shown in Fig. 3. The dynamics of the system, quantified by the fidelity of the instantaneous wave function of the system with the ideal target state, $F^T = |\langle \psi_T | \psi(t) \rangle|^2$, is shown in Fig. 3(a) for a four-qubit chain. Blue dots correspond to a Floquet simulation at stroboscopic times, which closely follow the red solid curve of the ideal continuous annealer. The blue curve shows the full dynamics. Since the fidelity is calculated in the computational basis, strong oscillations appear from the drives. These oscillations could be removed by changing to a suitable rotating basis. To study the scaling with the system size, we perform fixed time ($t_f = 15|J_{\text{sim}}|^{-1}$) annealing for chains of various lengths [Fig. 3(b)]. Fixing the drive frequency to moderate values, we observe that the final infidelities of the Floquet simulator, $1 - F_{\text{Floquet}}^c(t_f)$, and digital simulator, $1 - F_{\text{digital}}^c(t_f)$, have similar scaling with the system size, both adding extra infidelity on top of the continuous evolution and largely dependent on ω and N_{Tr} as described below. In Fig. 3(c), we show the dependence on the frequency of the periodic drive of the Floquet infidelity, measured with respect to the finite time annealing state. The frequency is rescaled by the total annealing time, such that $\omega t_f/2\pi$ shows the number of stroboscopic periods. The infidelity can be reduced for large ω , with results converging to continuous annealing for $\omega/|J| \rightarrow \infty$. The analogous behavior for the digital approach corresponds to the

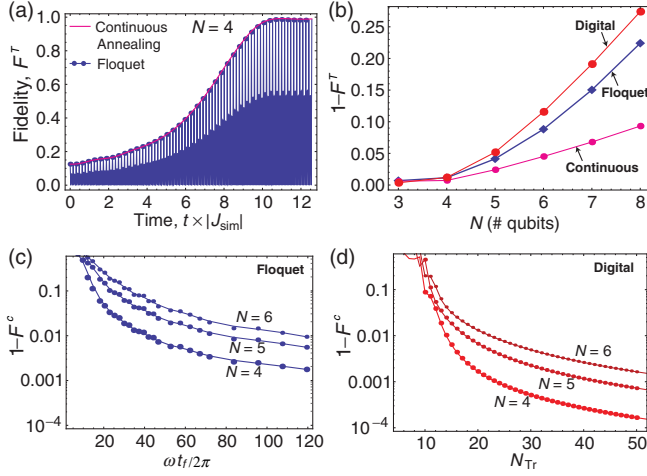


FIG. 3. *Transverse Ising annealing.* (a) Fidelity of the simulated state with respect to the ideal target state. The dark red line denotes annealing with the ideal transverse Ising Hamiltonian. The blue thin line corresponds to evolution under the time-dependent Hamiltonian, with blue dots showing state fidelities at accessible stroboscopic times. We assume $J_{\text{sim}} < 0$, $h^z/|J_{\text{sim}}| = 1$, $t_f = 12.5|J_{\text{sim}}|^{-1}$, and $\omega/|J| = 20$. (b) Final time infidelities $1 - F^T$ for ideal continuous, Floquet, and digital evolution shown for different numbers of qubits. Parameters are the same as in (a) with final simulation time $t_f = 15|J_{\text{sim}}|^{-1}$. The digital evolution corresponds to $N_{\text{Tr}} = 20$ Trotter steps. (c) Final infidelity $1 - F^c$ of the Floquet simulation as a function of the modulation frequency for $N = 4, 5, 6$. (d) Infidelity $1 - F^c$ of the digital annealing as a function of the number of Trotter steps for $N = 4, 5, 6$ qubits.

variation of the number of Trotter steps and is shown in Fig. 3(d). While a direct comparison between the two approaches is complicated, the general tendency can be deduced: The Floquet approach has smaller infidelity for a small number of steps and limited resources, while the digital approach has better scaling if a large number of Trotter steps N_{Tr} can be implemented.

C. Imperfections

1. Influence of finite anharmonicity

To describe a realistic quantum simulator, we study the influence of a finite anharmonicity A of the SC qubits, which will be a major limitation to our approach. Driving a transmon with a finite anharmonicity leads to the leakage of information from the logical subspace. To account for this, we consider a full Hamiltonian of a SC chain and perform numerical simulations including doubly excited states of the transmons. The full Hamiltonian reads

$$\hat{\mathcal{H}} = 2J \sum_{j=1}^{N-1} (\hat{a}_j^\dagger \hat{a}_{j+1} + \hat{a}_j \hat{a}_{j+1}^\dagger) + \sum_{j=1}^N \{ \Delta_j \hat{a}_j^\dagger \hat{a}_j + (\Omega_j \hat{a}_j + \Omega_j^* \hat{a}_j^\dagger) \} + \sum_{j=1}^N \frac{A}{2} \hat{a}_j^\dagger \hat{a}_j^\dagger \hat{a}_j \hat{a}_j, \quad (6)$$

where \hat{a}_j^\dagger (\hat{a}_j) corresponds to the creation (annihilation) operator for excitations of the j th transmon circuit. The first term in Eq. (6) corresponds to nearest-neighbor capacitive coupling for transmons. The second term in curly brackets denotes an effective magnetic field in the z direction given by the flux-bias-dependent detuning Δ_j and the microwave drive terms Ω_j corresponding to an effective magnetic field in the xy plane. The last term in Eq. (6) corresponds to the anharmonicity of the circuit A provided by Josephson junctions. In the case of infinitely large anharmonicity, the Hamiltonian (6) can be projected onto the lowest occupation subspace for each qubit $\{|0\rangle, |1\rangle\}_j$ accounting only for singly excited circuits. This allows for a spin-1/2 description of the chain and subsequent simulation of quantum magnetism as shown in the previous section. However, in realistic transmon samples, the anharmonicity is typically small, and higher states of the circuit must be accounted for [see the sketch in Fig. 4(a)]. In particular, this is important for the case of a strong microwave drive Ω , as it leads to nonzero occupation of higher-lying states and enhanced leakage. This can largely decrease the fidelity and typically is the bottleneck for fast digital computation.

In the following, we consider the effects of finite A by expanding the Hilbert space for each site to have doubly

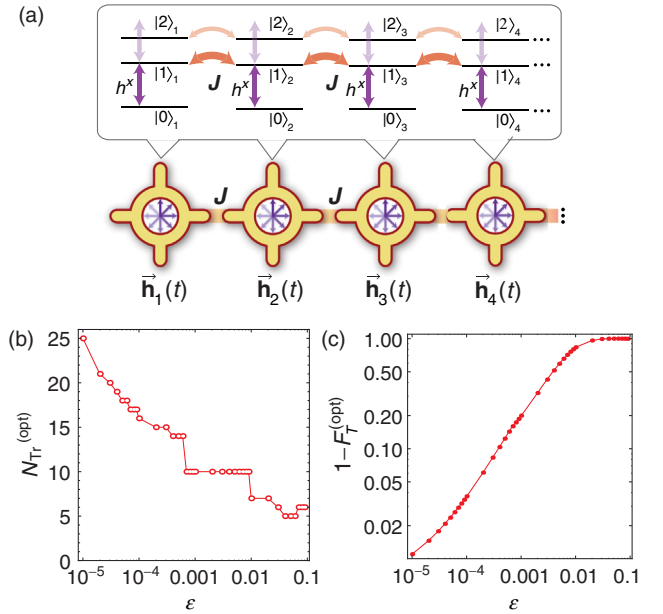


FIG. 4. *Accounting for finite anharmonicity.* (a) Sketch of a realistic transmon chain with weakly anharmonic multilevel structure. In each circuit, we account for $\{|0\rangle_j, |1\rangle_j, |2\rangle_j\}$ states. The infidelity of the simulation arises from microwave driving of the $|1\rangle_j \leftrightarrow |2\rangle_j$ transition and additional flip-flop coupling. (b) Optimal number of Trotter steps $N_{\text{Tr}}^{(\text{opt})}$ plotted for different values of the gate error. (c) Corresponding optimal infidelity as a function of the gate error. The results are shown for transverse Ising annealing with $t_f = 15|J|^{-1}$ and $N = 4$.

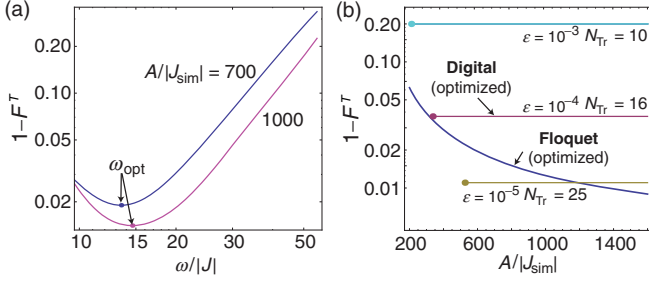


FIG. 5. *Imperfections.* (a) Infidelity of Floquet transverse Ising annealing ($N = 4$) with respect to the ideal target state calculated for a fixed anharmonicity and varying frequency. The point of low infidelity defines an optimal frequency for the simulation. (b) Final-state infidelity for transverse Ising annealing for $N = 4$, $\omega = \omega^{\text{opt}}$, and $t_f = 15|J|^{-1}$. The anharmonicity A spans the range $A/\omega = 19\text{--}99$. Horizontal lines show optimized digital protocol infidelities for fixed single-gate error ϵ , with the cutoff (large dots) determined by a minimal gate time $t_{\text{gate}} \geq 35A^{-1}$.

occupied states, $\{|0\rangle, |1\rangle, |2\rangle\}_j$. As a test case, we take the ground-state preparation of the transverse Ising model, studied for the case of infinite anharmonicity in the preceding sections. The annealing schedule is chosen in the same form, making use of the correspondence $h^x \leftrightarrow \Omega(\Omega^*)$ and $h^z \leftrightarrow 2\Delta$.

We consider annealing of the transverse Ising chain with $N = 4$. The resulting infidelity of the simulation is shown in Fig. 5. First, we fix the value of the anharmonicity and calculate the infidelity as a function of the Floquet frequency [Fig. 5(a)]. We observe that, contrary to the ideal circuit, the infidelity is minimized for a finite (optimal) drive frequency ω^{opt} . The window of frequencies in which the infidelity stays close to minimal is typically broad. In Fig. 5(b), we show the optimized infidelity of the simulation as a function of A (blue curve).

To benchmark the results of the Floquet simulation, we compare it to the digital simulation. The estimate of the digital protocol infidelity accounts for several contributions. The first comes from the Trotterization procedure $\epsilon_{\text{dig}}(N_{\text{Tr}})$ and depends strongly on the number of Trotter steps, favoring long sequences. The second contribution is a total infidelity from gate operations $\epsilon_{\text{gates}}(N_{\text{Tr}}) = 1 - [1 - (5N - 4)\epsilon]^{N_{\text{Tr}}}$, which increases with the number of Trotter steps. The optimization procedure is performed for different values of the gate error ϵ . The results are plotted in Fig. 4(b), and the optimal Trotter step number $N_{\text{Tr}}^{\text{opt}}$ is shown to decrease in the case of large gate errors. The corresponding optimal infidelity [Fig. 4(c)] shows a significant increase for $\epsilon > 10^{-3}$.

To compare the digital and Floquet approaches, we should compare how each of the two approaches could be implemented on comparable physical systems. To this end, we consider transmons with the same anharmonicity A and assume that they also have comparable decoherence

rates (but note that we assume that the physical coupling J can be different in the two scenarios). Therefore, to have a similar influence of decoherence in the two approaches, we assume that the simulations need to be completed in the same time. To simulate the same evolution, this requires that the two approaches have the same J_{sim} and, thus, the same values of A/J_{sim} . In the Floquet case, this is defined by the A/ω and ω/J ratios. For the digital simulation, the relation is more subtle and relies on the scaling of the gate time with A for a fixed error value. A full discussion of this complex subject lies beyond the scope of present study, and for simplicity we just assume that each gate can be implemented in a time $t_{\text{gate}} = c/A$, where c is a constant which controls the quality of the gate. Taking the existing studies [53–55] and considering a best-case scenario, we set $c = 35$. For realistic devices with $A = 2\pi \times 300$ MHz, this will correspond to 18-ns gates.

Assuming the same value ϵ for the single- and two-qubit errors, the error for a single Trotter step is equal to $\epsilon_{\text{Tr}} = (5N - 4)\epsilon$. We optimize the total infidelity $1 - F_{\text{tot}}^T = 1 - (1 - \epsilon_{\text{Tr}})^{N_{\text{Tr}}}(1 - \epsilon_{\text{dig}})$ with respect to the number of Trotter steps, using the data shown in Fig. 4. To highlight the relevant parameter range, we assign a cutoff based on the single-gate time $t_{\text{gate}} \geq 35A^{-1}$. The results are plotted as horizontal lines in Fig. 5(b) and show that the Floquet approach can outperform the digital approach unless very-high-fidelity gates with $\epsilon < 10^{-4}$ are used. Furthermore, the Floquet approach is highly advantageous for small values of A/J_{sim} , which for a given transmon anharmonicity A is the regime where the simulation is finished the fastest and thus has the least influence of decoherence. Thus, for a shorter time of simulation or higher error rates, the Floquet is advantageous compared to the digital approach. We highlight that, while digital approaches typically exploit derivative reduction by adiabatic gate (DRAG) technique to remove leakage [54,55], the presented Floquet approach is not specifically designed to work for small A , and it may be improved by using few-tone drives.

To quantify the performance, we consider numbers which can be achieved with currently available transmon setups [47,49]. Taking the anharmonicity to be $A = 2\pi \times 300$ MHz, drive frequency $\omega = 2\pi \times 9.8$ MHz, nearest-neighbor coupling $J = 2\pi \times 1$ MHz (reduced compared to most setups), and $t_f = 2.4 \mu\text{s}$, the four-qubit chain can be annealed to the ground state of the Ising model with $1 - F_{\text{Flq}}^T = 0.037$ (ideal continuous annealing gives $1 - F_{\text{cont}}^T = 0.00616$).

Reaching a similar performance with the digital strategy is highly challenging and would require single- and two-qubit gate operation times of $18 \text{ ns} = 35A^{-1}$ and $\epsilon = 10^{-4}$ accuracy. The single Trotter step duration for $N = 4$ is $t_{\text{Tr}} = 0.162 \mu\text{s}$, and with $t_f = 2.4 \mu\text{s}$ this allows for 14 Trotter steps. The total digital error is $1 - F_{\text{dig}} = 0.041$ (dephasing should be added separately).

2. Influence of the coupling to the environment

So far, we have considered the situation where the dynamics of the quantum system is unitary and errors arise due to the difference between the target Hamiltonian and the effective Floquet Hamiltonian engineered by the drive. In realistic setups, errors also appear due to the coupling to the environment, so that a qubit can decay, or its state can be dephased by the external noise. To account for the environmental contribution, we perform a master-equation simulation for the density matrix ρ of the superconducting qubit chain, $\dot{\rho}(t) = -i[\hat{H}(t), \rho(t)] + \hat{D}[\rho(t)]$. Assuming that each qubit can decay due to the collapse operator $\hat{C}_j = \sqrt{\gamma}\sigma_j^-$ with a rate γ , the decoherent part of the dynamics is described by the Liouvillian superoperator $\hat{D}[\rho] = \sum_{j=1}^N \hat{C}_j \rho \hat{C}_j^\dagger - \{\hat{C}_j^\dagger \hat{C}_j, \rho\}/2$. Here γ corresponds to the Markovian decay rate, and we assume a zero temperature of the bath, which is justified for modern experiments performed at $T \approx 25$ mK, with $k_B T$ being much smaller than the qubit frequency (approximately 5 GHz). We note that, even though we assume the environment to be at a zero temperature, the application of the strong driving fields creates a nonequilibrium situation. In the effective model, this decay will thus not correspond to a zero-temperature bath [56]. Furthermore, we note that pure dephasing effects can be included in a similar fashion.

To study the performance of the simulator under the influence of environmental effects, we consider the benchmarking example of annealing to the ground state of the transverse Ising Hamiltonian. We calculate the infidelity $1 - F^T$ of the continuous finite time annealing and Floquet annealing, measured with respect to the ideal GHZ target state, as a function of the qubit decay. The parameters used are $\omega/|J| = 20$ and $t_f = 15|J_{\text{sim}}|^{-1}$, and we consider a chain with $N = 4$ qubits. The results are shown in Fig. 6. Taking the circuit considered in the previous subsection ($A = 2\pi \times 300$ MHz, $J = 2\pi \times 1$ MHz), we find

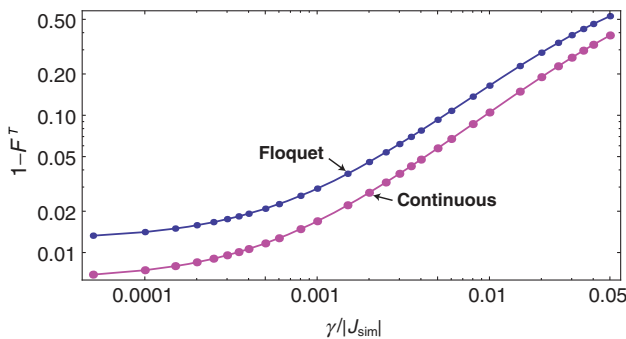


FIG. 6. *Influence of decay.* Final-state infidelity for annealing to the ground state of the transverse Ising model, shown as a function of qubit decay rate γ . Continuous annealing (magenta curves) and Floquet annealing (blue curves) are considered, with fidelity measured with respect to the ideal target state. The parameters are $N = 4$, $\omega/|J| = 20$, and $t_f = 15|J_{\text{sim}}|^{-1}$.

that, for qubits with $T_1 = 10 \mu\text{s}$ decay time, the infidelity of GHZ state preparation becomes $1 - F_{\text{Flq}}^T = 0.248$. Even in the absence of decay, the Floquet protocol has a larger error, since we consider a finite $\omega/|J|$. As expected, the addition of the decay increases the infidelity for both continuous and Floquet annealing. Although the scaling looks similar on the log-log scale, it corresponds to a more rapid growth of decoherence-related infidelity for the Floquet approach at large decay rates. The presence of decay leads to another trade-off, favoring large coupling J_{sim} , at the expense of leakage and Floquet errors, but we have not included this in our optimizations. Finally, we note that the described annealing protocol is resource demanding, as it requires long simulation time t_f to achieve a high fidelity even in the ideal unitary case, while dynamical simulations can be performed in a much shorter time, thus having less effects of decoherence.

3. Influence of cross talk between neighboring qubits

In ideal transmon circuits, each qubit has a separate independently controllable microwave and flux loop lines, which allow engineering the effective magnetic field. However, in realistic samples, the microwave lines can have an additional capacitive coupling to neighboring qubits, thus providing an extra drive [57]. This parasitic or “cross-talk” coupling may have a harmful influence on the effective Hamiltonian. If these cross talks are completely known for the sample at hand, one can always compensate for this by adding extra drives to each qubit which counteract the cross talk. In practice, however, we may not have a complete characterization of the sample, and this introduces errors in the protocol.

Here, we study the influence of cross-couplings on the performance of the simulator, providing estimates for the associated infidelity of the simulation. Taking the example of annealing to the ground state of the transverse Ising Hamiltonian, the Floquet approach requires an x -oriented periodic drive for each second qubit (e.g., even sites), while odd sites are not driven. Using the drive parameters introduced in Appendix A, this situation corresponds to $\phi_e = 0$, $\theta_e = \pi/2$, $\phi_o = 0$, $\theta_o = \pi/2$, and ideally $\lambda_o = 0$. The presence of nonzero cross-talk coefficients results in the appearance of an additional drive, such that $\lambda_o = \mathbf{c}\lambda_e$, where \mathbf{c} is a cross-talk coefficient, which may be different for each link, $\mathbf{c} \rightarrow \{c_l\}$ [see the sketch in Fig. 7(a)]. Using the generic model given by Eq. (4), with the coefficients written in Appendix A, we can write the interaction constants as

$$\overline{\xi_{xx}}/J = 1, \quad \overline{\xi_{yy}}/J = \frac{1}{2}(\mathcal{J}_0[\lambda_e - \lambda_o] + \mathcal{J}_0[\lambda_e + \lambda_o]), \quad (7)$$

$$\overline{\xi_{zz}}/J = \frac{1}{2}(\mathcal{J}_0[\lambda_e - \lambda_o] - \mathcal{J}_0[\lambda_e + \lambda_o]), \quad (8)$$

and other interaction constants are zero: $\overline{\xi_{xy}}/J = \overline{\xi_{yz}}/J = \overline{\xi_{xz}}/J = 0$. Assuming the cross-talk coefficients to be small,

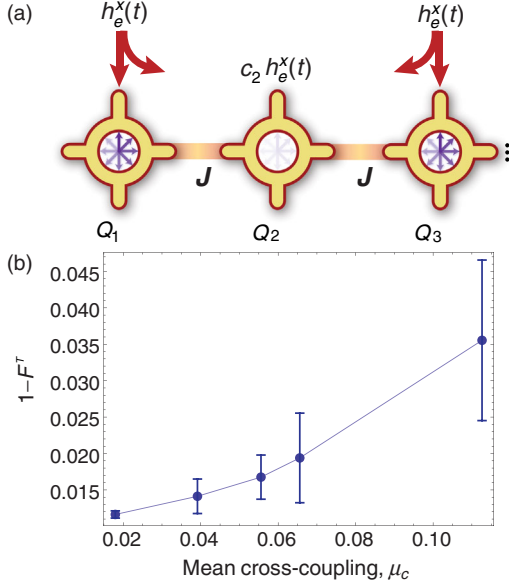


FIG. 7. *Influence of cross talk.* Final-state infidelity for annealing to the ground state of the transverse Ising model as a function of the mean cross-talk coefficient μ_c . The calculation is performed for several sets of cross-coefficients drawn from the half-normal distribution with different μ_c . The error bar shows one standard deviation of the calculated infidelity of the sample; i.e., it represents the fluctuations expected between different devices. The curve is calculated using 20 sets of the cross-couplings. Other parameters are $\omega/|J| = 20$, $t_f = 15|J_{\text{sim}}|^{-1}$, and $N = 4$.

$\bar{c} \ll 1$, we can expand YY and ZZ interaction constants, arriving at

$$\frac{\overline{\xi_{yy}}}{J} = \mathcal{J}_0[\lambda_e] + \left\{ \frac{\lambda_o^2}{2\lambda_e} \mathcal{J}_1[\lambda_e] - \frac{\lambda_o^2}{2} \mathcal{J}_0[\lambda_e] \right\} + \mathcal{O}(\lambda_o)^3, \quad (9)$$

$$\frac{\overline{\xi_{zz}}}{J} = \lambda_o \mathcal{J}_1[\lambda_e] + \mathcal{O}(\lambda_o)^3, \quad (10)$$

where additional terms appear due to nonzero λ_o . The first term in (9) corresponds to the leading λ_e -based contribution, and to achieve the Ising Hamiltonian coupling we tune $\lambda_e \rightarrow \lambda_0$, where $\mathcal{J}_0[\lambda_0] = 0$. This leaves only the residual term for $\overline{\xi_{yy}}/J \approx (\lambda_o^2/2\lambda_0)^2 \mathcal{J}_1[\lambda_0] \approx 0.11\lambda_o^2$, which is typically negligible for small cross-talk coefficients. At the same time, an effective ZZ coupling arises to first order, giving $\overline{\xi_{zz}}/J \approx \lambda_o \mathcal{J}_1[\lambda_0] \approx 0.52\lambda_o$. We note, however, that knowing the cross-talk coefficients can enable fine-tuning the interaction such that $\overline{\xi_{zz}}/J$ is minimized.

Finally, to account for the randomly distributed cross talk $\{c_l\}$, we perform numerical calculation of the annealing to the transverse Ising Hamiltonian ground state including the cross talk. The coefficients $\{c_l\}$ are drawn from the half-normal distribution. They correspond to the set of absolute values of random variables $\{|x_l|\}$ drawn from the normal distribution with $P_{\text{normal}}(x; \sigma) = \sqrt{2/(\pi\sigma^2)} \exp(-x^2/2\sigma^2)$ (σ^2

is the variance of the normal distribution). Then, $\mu_c = \sum_l^L c_l/L$ is calculated as an arithmetic mean for the sample, where L is the total sample size. The choice of positive coefficients is determined by the fact that cross talk is typically represented by the passive capacitive coupling and does not change the sign of the parasitic magnetic field on the nondriven sites. We also check the case where this situation may not hold, taking the normal distribution with a zero mean and the same σ , and find that the associated infidelity in the simulation is of a comparable size.

We choose to plot the results as a function of mean cross-coupling μ_c . The infidelity with respect to the target state is shown in Fig. 7(b). The sampling is performed for $\omega/|J| = 20$, $t_f = 15|J_{\text{sim}}|^{-1}$, and $N = 4$ and considering 20 cross-talk configurations. The infidelity naturally grows for increasing values of the cross-coupling. Taking, for instance, a mean cross talk of 5%, we find the additional infidelity to be around 0.015.

Finally, concluding the imperfections section, we note that Floquet systems can suffer from induced heating even for isolated setups [58]. This is related to an effective breakdown of the Magnus expansion for systems of a large size, where characteristic energy spacing becomes small. However, the latter concerns the thermodynamic limit and happens at critical times being exponentially large in the drive frequency [59,60].

D. Generic XYZ Hamiltonians

The Floquet approach may be extended to simulate generic spin-1/2 models represented by XYZ -type spin Hamiltonians, $\hat{\mathcal{H}}_{XYZ} = \sum_{j=1}^{N-1} (J^x \sigma_j^x \sigma_{j+1}^x + J^y \sigma_j^y \sigma_{j+1}^y + J^z \sigma_j^z \sigma_{j+1}^z)$. This coupling is of the nonstoquastic type, where recent results have suggested that it can give enhanced computational powers [61]. To simulate the XYZ model in the Floquet basis, we start with the time-dependent Hamiltonian in the form

$$\hat{\mathcal{H}}(t) = \sum_{j=1}^{N-1} J(\sigma_j^x \sigma_{j+1}^x + \sigma_j^y \sigma_{j+1}^y) + \sum_{j=1}^N \mathbf{h}(t) \cdot \boldsymbol{\sigma}_j + \hat{\mathcal{H}}_z, \quad (11)$$

where we consider the oscillating effective magnetic field to be homogeneous for all sites. $\hat{\mathcal{H}}_z$ describes the part of the Hamiltonian responsible for implementing the static z -oriented magnetic field for annealing. Considering $\mathbf{h}(t) = (\lambda/2)\omega \cos(\omega t) \mathbf{e}^x$ with ω being the largest energy scale and setting $\lambda = 3.62288$, we eliminate the cross terms and are left with a Floquet Hamiltonian of the form

$$\hat{\mathcal{H}}_F = \sum_{j=1}^{N-1} (J^x \sigma_j^x \sigma_{j+1}^x + J^y \sigma_j^y \sigma_{j+1}^y + J^z \sigma_j^z \sigma_{j+1}^z) \quad (12)$$

$$+ h^z \sum_{j=1}^N \sigma_j^z \equiv \hat{\mathcal{H}}_{XYZ}, \quad (13)$$

where the couplings are $J^y = 2J^x/3$, $J^z = J^x/3$, and $J^x = J < 0$. Here the simulated coupling changes for the YY and ZZ interaction components, and we consider $J^x = J_{\text{sim}}$ as a reference. We note that, as compared to the transverse Ising case, this Hamiltonian possesses a small energy gap, and in the absence of an additional transverse field it is difficult to anneal even with the ideal continuous Hamiltonian.

To characterize the Floquet and digital simulation procedures, we plot the instantaneous infidelity with respect to the continuous annealing case, observing how closely one can follow the ground state [Fig. 8(a)]. The blue curve for the Floquet simulation at stroboscopic times shows that the deviation begins to grow once we approach the critical point. To compare with the digital procedure [see Appendix D for details], we plot the infidelity for the Trotterization approach. We assume the number of Trotter steps is equal to half of number of Floquet periods, $N_{\text{Tr}} = 1/2(t_f/T) = 477$. This will be an upper bound for the number of Trotter steps for the digital simulator for the same resources. This can be deduced from the digital simulation protocol, assuming that the time required to implement the two-qubit gate is inversely proportional to the coupling strength, $t_{\text{gate}} \sim |J|^{-1}$, and, in addition, the

gates on the two sublattices have to be applied separately. We note that considering different ordering of the gates leads to largely different results for the final-state infidelity. While we have not performed a full optimization of this ordering, the results presented in the figure are the outcome of the optimization over 24 different possibilities for a Trotter step composition. This suggests that the digital procedure is strongly model dependent, and extra resources are required for sequence optimization [2,4]. In Fig. 8(b), we plot the dependence of the Floquet XYZ annealing on the drive frequency, showing the resources necessary for high-fidelity annealing as a function of the number of stroboscopic periods. A similar analysis is performed for the digital procedure, where the dependence of the Trotter step number is considered [Fig. 8(c)]. Akin to the transverse Ising annealing case described in the previous sections, the Floquet approach shows a smaller infidelity for a limited number of steps, in particular, for $N = 4$. Unlike the transverse Ising model, however, even for N_{Tr} as large as a thousand steps, the digital approach does not provide a smaller infidelity as compared to the Floquet approach, but this may change if even higher numbers of Trotter steps are considered.

IV. CONCLUSIONS

In conclusion, we presented a scheme for a reconfigurable and tunable superconducting quantum simulator based on transmon qubits. Utilizing the Floquet approach, the original isotropic XY interaction can be transformed into a transverse Ising or XYZ -type spin-1/2 Hamiltonian. The approach allows the simulation of multiqubit system dynamics and the preparation of nontrivial ground states. The Floquet simulation is shown to perform better than a digital scheme for restricted resources and represents a realistic path for modern SC quantum simulators.

ACKNOWLEDGMENTS

The research is funded by the European Union Seventh Framework Program through ERC Grant QIOS (Grant No. 306576). O. K. acknowledges useful discussions with Pedram Roushan, Charles Neill, Guanyu Zhu, Mohammad Hafezi, Göran Johansson, and Stefan Filipp.

APPENDIX A: DERIVATION OF THE GENERIC FLOQUET HAMILTONIAN

Here we present the derivation of Eq. (4) in the main text and simultaneously describe the general Floquet Hamiltonian originating from an arbitrary axis magnetic-field oscillation for the two sublattices.

We start with the transmon Hamiltonian written in the form

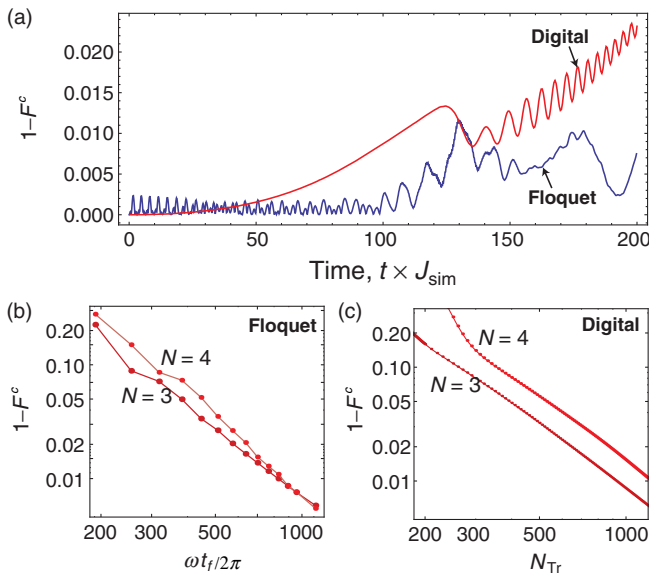


FIG. 8. *XYZ annealing*. (a) Time dependence of the infidelity for the Floquet evolution (blue line) and optimal digital annealing (red line). Here the infidelity is measured with respect to the instantaneous wave function of the continuous annealing. The digital evolution contains $N_{\text{Tr}} = 477$ Trotter steps, equal to half the number of stroboscopic periods. (b) Modulation frequency dependence of the final-state infidelity for annealing with $t_f = 200|J|^{-1}$, measured with respect to an ideal target state. (c) Final infidelity of the digital quantum simulation of the XYZ model as a function of the number of Trotter steps. F is measured with respect to an ideal target state.

$$\begin{aligned}
\hat{\mathcal{H}}(t) &= \hat{\mathcal{H}}_0 + \hat{\mathcal{H}}_1(t) \\
&= J \sum_{j=1}^{N-1} (\sigma_j^x \sigma_{j+1}^x + \sigma_j^y \sigma_{j+1}^y) + \sum_{j=1}^{\lfloor N/2 \rfloor} \mathbf{h}_{\text{odd}}(t) \cdot \boldsymbol{\sigma}_{2j-1} \\
&\quad + \sum_{j=1}^{\lfloor N/2 \rfloor} \mathbf{h}_{\text{even}}(t) \cdot \boldsymbol{\sigma}_{2j} \quad (\text{A1})
\end{aligned}$$

and consider the effective magnetic fields to be different for even and odd sublattices. Here $\lfloor x \rfloor$ and $\lceil x \rceil$ denote floor and ceiling functions, correspondingly. To have an explicit form of $\mathbf{h}_{\text{even/odd}}(t)$, we decompose it into $\mathbf{h}_{\text{even/odd}}(t) = f_{e/o}(t)(\mathbf{e}^x h_{e/o}^x + \mathbf{e}^y h_{e/o}^y + \mathbf{e}^z h_{e/o}^z)$, where $f_{e/o}(t) = f_{e/o}(t+T)$ is some periodic function, $\mathbf{e}^{x,y,z}$ form a Cartesian basis, and $h_{e/o}^\alpha$ are components of an effective magnetic field for even (indexed by e) and odd (indexed

by o) sites. This corresponds to the magnetic field oscillating along a certain axis, which is different for even and odd sublattices. Here we consider the time dependence to be the same for all spin components, such that the axis of the magnetic field does not precess. This restriction decreases the number of independent tuning parameters. Note that the effective magnetic field used for the simulation of the transverse Ising model deviates slightly from this form. This deviation is, however, a perturbation and is dealt with below. If the fields do not have this form, the time-dependent Hamiltonian $\hat{\mathcal{H}}_1(t)$ does not commute with itself at different times, thus largely complicating the solution. This more general setting will be considered in future work.

We perform a unitary transformation with respect to the rapidly oscillating time-dependent part $\hat{\mathcal{H}}_1(t)$. This is done using the unitary operator:

$$\hat{\mathcal{U}}(t) = \mathcal{T} \exp \left[-i \int_{t_0}^t dt' f_o(t') \sum_{j=1}^{\lfloor N/2 \rfloor} (h_o^x \sigma_{2j-1}^x + h_o^y \sigma_{2j-1}^y + h_o^z \sigma_{2j-1}^z) + f_e(t') \sum_{j=1}^{\lfloor N/2 \rfloor} (h_e^x \sigma_{2j}^x + h_e^y \sigma_{2j}^y + h_e^z \sigma_{2j}^z) \right], \quad (\text{A2})$$

where $\hat{\mathcal{T}}\{\dots\}$ is the time-ordering operator and t_0 is an initial switch-on time. The unitary (A2) can be factorized into odd and even sublattices parts, and time ordering disappears as the magnetic field oscillates along a fixed axis. This yields $\hat{\mathcal{U}}(t) = \hat{\mathcal{U}}_o(t) \hat{\mathcal{U}}_e(t)$ with

$$\hat{\mathcal{U}}_p(t) = \exp \left[-i \frac{g_p(t)}{2} \sum_{j=1}^{N_p} (n_p^x \sigma_p^x + n_p^y \sigma_p^y + n_p^z \sigma_p^z) \right], \quad (\text{A3})$$

where indices $p = o, e$ and $P=2j-1, 2j$ help denote sublattice parity, and we define the time-integrated functions $g_p(t) \equiv 2 \int_{t_0}^t dt' f_p(t') h_p$. Here $h_p = \sqrt{(h_p^x)^2 + (h_p^y)^2 + (h_p^z)^2}$ defines the absolute value of the effective magnetic-field vector, and $n_p^{x,y,z} = h_p^{x,y,z} / h_p$

correspond to the normalized Cartesian components. The rotated Hamiltonian then reads $\hat{\mathcal{H}}'(t) = \hat{\mathcal{U}}^\dagger(t) \hat{\mathcal{H}}(t) \hat{\mathcal{U}}(t) - i \hat{\mathcal{U}}^\dagger(t) \partial_t \hat{\mathcal{U}}(t)$. The second term is divided into two parts and each of these can be rewritten using the relation for the derivative of an arbitrary time-dependent matrix $A(t)$, being $e^{-A(t)} \partial_t e^{A(t)} = \dot{A}(t) - [A(t), \dot{A}(t)]/2! + [A(t), [A(t), \dot{A}(t)]]/3! - \dots$. For the case of $A(t) = -i \{ [g_p(t)]/2 \} \sum_{j=1}^{N_p} (n_p^x \sigma_p^x + n_p^y \sigma_p^y + n_p^z \sigma_p^z)$ considered here, the commutators vanish, and in total the derivative term gives $-\hat{\mathcal{H}}_1(t)$. However, we emphasize that this conclusion would not be true for general time dependence of the Cartesian components of an effective magnetic field, where additional derivative-dependent terms appear.

Next, we need to calculate the matrix product terms of the form

$$\begin{aligned}
&\hat{\mathcal{U}}^\dagger(t) \left[J \sum_{j=1}^{N-1} (\sigma_j^x \sigma_{j+1}^x + \sigma_j^y \sigma_{j+1}^y) \right] \hat{\mathcal{U}}(t) \\
&= e^{\{i[g_e(t)/2] \sum_{j=1}^{N_e} (n_e^x \sigma_{2j}^x + n_e^y \sigma_{2j}^y + n_e^z \sigma_{2j}^z)\}} e^{\{i[g_o(t)/2] \sum_{j=1}^{N_o} (n_o^x \sigma_{2j-1}^x + n_o^y \sigma_{2j-1}^y + n_o^z \sigma_{2j-1}^z)\}} \\
&\quad \times \left[J \sum_{j=1}^{N-1} (\sigma_j^x \sigma_{j+1}^x + \sigma_j^y \sigma_{j+1}^y) \right] e^{\{-i[g_o(t)/2] \sum_{j=1}^{N_o} (n_o^x \sigma_{2j-1}^x + n_o^y \sigma_{2j-1}^y + n_o^z \sigma_{2j-1}^z)\}} e^{\{-i[g_e(t)/2] \sum_{j=1}^{N_e} (n_e^x \sigma_{2j}^x + n_e^y \sigma_{2j}^y + n_e^z \sigma_{2j}^z)\}}. \quad (\text{A4})
\end{aligned}$$

Let us perform the unitary rotation for each sublattice consecutively. For this, it is convenient to go from Cartesian to the spherical coordinate frame: $\mathbf{n}_p = \{n_p^x, n_p^y, n_p^z\} \leftrightarrow \{\cos \phi_p \sin \theta_p, \sin \phi_p \sin \theta_p, \cos \theta_p\}$. Next, noting that the unitary operation is defined as a spin rotation with respect to a fixed axis \mathbf{n}_p , it can be decomposed into Cartesian rotations as

$$\hat{\mathcal{R}}_j^{\mathbf{n}}(g) = e^{-i(g/2)\mathbf{n}\cdot\sigma_j} = \hat{\mathcal{R}}_j^z(\phi)\hat{\mathcal{R}}_j^y(\theta)\hat{\mathcal{R}}_j^z(g)\hat{\mathcal{R}}_j^y(\theta)^\dagger\hat{\mathcal{R}}_j^z(\phi)^\dagger, \quad (\text{A5})$$

where the rotation operator is defined as $\hat{\mathcal{R}}^\alpha(\varphi) = e^{-i(\varphi/2)\sigma^\alpha}$ ($\alpha = x, y, z$). Then, the Hamiltonian after the odd sublattice transformation can be obtained through rotations

$$\hat{\mathcal{U}}^\dagger(t)\hat{\mathcal{H}}_0\hat{\mathcal{U}}(t) = \hat{\mathcal{U}}_e^\dagger[\hat{\mathcal{R}}_o^z(\phi_o)\hat{\mathcal{R}}_o^y(\theta_o)\hat{\mathcal{R}}_o^z(-g_o)\hat{\mathcal{R}}_o^y(-\theta_o)\hat{\mathcal{R}}_o^z(-\phi_o)\hat{\mathcal{H}}_0\hat{\mathcal{R}}_o^z(\phi_o)\hat{\mathcal{R}}_o^y(\theta_o)\hat{\mathcal{R}}_o^z(g_o)\hat{\mathcal{R}}_o^y(-\theta_o)\hat{\mathcal{R}}_o^z(-\phi_o)]\hat{\mathcal{U}}_e, \quad (\text{A6})$$

and the subsequent transformation for the even sublattice can be performed in a similar fashion.

Finally, to get a closed expression for the transformed Hamiltonian, we use the Baker-Campbell-Hausdorff formula

$$e^{\hat{\mathcal{M}}}\hat{\mathcal{H}}_0e^{-\hat{\mathcal{M}}} = \hat{\mathcal{H}}_0 + [\hat{\mathcal{M}}, \hat{\mathcal{H}}_0] + \frac{1}{2!}[\hat{\mathcal{M}}, [\hat{\mathcal{M}}, \hat{\mathcal{H}}_0]] + \dots = \sum_{k=0}^{\infty} \frac{1}{k!}[\hat{\mathcal{M}}, \hat{\mathcal{H}}_0]_k, \quad (\text{A7})$$

where $[\hat{\mathcal{M}}, \hat{\mathcal{H}}_0]_k$ denotes the k th-order nested commutator. We proceed with calculating the commutators and resumming the series. After straightforward but tedious algebra, we can get the Hamiltonian in a rotating frame:

$$\hat{\mathcal{H}}'(t) = \sum_{\alpha, \alpha' = x, y, z} \sum_{j=1}^{N/2} \xi_{\alpha\alpha'} \sigma_{2j}^\alpha (\sigma_{2j-1}^{\alpha'} + \sigma_{2j+1}^{\alpha'}), \quad (\text{A8})$$

with the coefficients

$$\begin{aligned} \xi_{xx}(t) &= J \sin^2(\theta_e) \cos(\phi_e) [\cos(g_o[t]) \cos^2(\theta_o) \cos(\phi_o) \cos(\phi_e - \phi_o) - \sin(\phi_e) \sin(g_o[t]) \cos(\theta_o) \\ &\quad - \cos(g_o[t]) \sin(\phi_o) \sin(\phi_e - \phi_o) + \sin^2(\theta_o) \cos(\phi_o) \cos(\phi_e - \phi_o)] \\ &\quad + \cos(g_e[t]) \{ \cos(g_o[t]) [\cos^2(\theta_o) \cos(\phi_o) (\cos^2(\theta_e) \cos(\phi_e) \cos(\phi_e - \phi_o) + \sin(\phi_e) \\ &\quad \times \sin(\phi_e - \phi_o)) + \sin(\phi_o) (\sin(\phi_e) \cos(\phi_e - \phi_o) - \cos^2(\theta_e) \cos(\phi_e) \sin(\phi_e - \phi_o))] \\ &\quad + \sin^2(\theta_e) \sin(\phi_e) \cos(\phi_e) \sin(g_o[t]) \cos(\theta_o) + \cos^2(\theta_e) \cos(\phi_e) \sin^2(\theta_o) \cos(\phi_o) \cos(\phi_e - \phi_o) \\ &\quad + \sin(\phi_e) \sin^2(\theta_o) \cos(\phi_o) \sin(\phi_e - \phi_o) \} + \sin(g_e[t]) \cos(\theta_e) \left[\sin(g_o[t]) \cos(\theta_o) - \sin^2\left(\frac{g_o[t]}{2}\right) \sin^2(\theta_o) \sin(2\phi_o) \right], \\ \xi_{yy}(t) &= J \sin^2(\theta_e) \sin(\phi_e) [\sin(\phi_o) \cos(\phi_e - \phi_o) (\cos(g_o[t]) \cos^2(\theta_o) + \sin^2(\theta_o)) + \cos(\phi_e) \sin(g_o[t]) \cos(\theta_o) \\ &\quad + \cos(g_o[t]) \cos(\phi_o) \sin(\phi_e - \phi_o)] + \cos(g_e[t]) \{ \cos(g_o[t]) [\cos^2(\phi_e) (\cos^2(\theta_o) \sin^2(\phi_o) + \cos^2(\phi_o)) \\ &\quad + \cos^2(\theta_e) \sin(\phi_e) (\cos^2(\theta_o) \sin(\phi_o) \cos(\phi_e - \phi_o) + \cos(\phi_o) \sin(\phi_e - \phi_o))] \\ &\quad + \sin(\phi_e) \cos(\phi_e) \sin^2(\theta_o) \sin(\phi_o) \cos(\phi_o)] - \sin^2(\theta_e) \sin(\phi_e) \cos(\phi_e) \sin(g_o[t]) \cos(\theta_o) \\ &\quad + \sin^2(\theta_o) \sin(\phi_o) (\cos^2(\theta_e) \sin(\phi_e) \cos(\phi_e - \phi_o) - \cos(\phi_e) \sin(\phi_e - \phi_o)) \} + \sin(g_e[t]) \cos(\theta_e) \\ &\quad \times \left[\sin(g_o[t]) \cos(\theta_o) + \sin^2\left(\frac{g_o[t]}{2}\right) \sin^2(\theta_o) \sin(2\phi_o) \right], \\ \xi_{zz}(t) &= J \sin(\theta_e) \sin(\theta_o) \left\{ \cos(\phi_e - \phi_o) \left[\sin(g_e[t]) \sin(g_o[t]) + 2(1 - \cos(g_e[t])) \cos(\theta_e) \sin^2\left(\frac{g_o[t]}{2}\right) \cos(\theta_o) \right] \right. \\ &\quad \left. + \sin(\phi_e - \phi_o) \left[(1 - \cos(g_e[t])) \cos(\theta_e) \sin(g_o[t]) - 2 \sin(g_e[t]) \sin^2\left(\frac{g_o[t]}{2}\right) \cos(\theta_o) \right] \right\}, \end{aligned}$$

$$\begin{aligned} \xi_{xy}(t) = & J \sin^2(\theta_o) \sin(\phi_o) [\cos(g_e[t]) (\cos^2(\theta_e) \cos(\phi_e) \cos(\phi_e - \phi_o) + \sin(\phi_e) \sin(\phi_e - \phi_o)) + \sin^2(\theta_e) \cos^2(\phi_e) \cos(\phi_o)] \\ & + \sin^2(\phi_o) \left[\sin^2(\theta_e) \cos^2(\phi_e) \sin(g_o[t]) \cos(\theta_o) + \frac{1}{2} \sin^2(\theta_o) (\sin^2(\theta_e) \sin(2\phi_e) - 2 \sin(g_e[t]) \cos(\theta_e)) \right] \\ & + \sin(g_o[t]) \cos(\theta_o) \times [\cos^2(\phi_e) (\cos(g_e[t]) \cos^2(\theta_e) + \sin^2(\theta_e) \cos^2(\phi_o)) + \cos(g_e[t]) \sin^2(\phi_e)] \\ & + \frac{1}{4} \cos(g_o[t]) \left[4 \cos(g_e[t]) \cos^2(\theta_e) \cos(\phi_e) \cos(\phi_o) \times (\sin(\phi_e) \cos(\phi_o) - \cos(\phi_e) \sin^2(\theta_o) \sin(\phi_o)) \right. \\ & + 4 \sin^2\left(\frac{g_e[t]}{2}\right) \sin^2(\theta_e) \sin(2\phi_e) \cos^2(\theta_o) \sin^2(\phi_o) + 4 \sin(\phi_e) \cos(\phi_e) \cos^2(\phi_o) (\sin^2(\theta_e) - \cos(g_e[t])) \\ & \left. - 4 \sin^2(\theta_o) \sin(\phi_o) \cos(\phi_o) (\cos(g_e[t]) \sin^2(\phi_e) + \sin^2(\theta_e) \cos^2(\phi_e)) - \sin(g_e[t]) \cos(\theta_e) \right. \\ & \left. \times (2 \sin^2(\theta_o) \cos(2\phi_o) + \cos(2\theta_o) + 3) \right], \end{aligned}$$

$$\begin{aligned} \xi_{yx}(t) = & J \frac{1}{8} \{ 8 \sin(g_e[t]) \cos(\theta_e) \sin^2(\theta_o) \cos^2(\phi_o) + 8 \cos(g_e[t]) \sin^2(\theta_o) \sin(\phi_o) \cos(\phi_o) (\cos^2(\theta_e) \sin^2(\phi_e) + \cos^2(\phi_e)) \\ & + 2 \cos(g_o[t]) [4 \cos^2(\theta_o) \cos(\phi_o) (\sin^2(\theta_e) \sin(\phi_e) \cos(\phi_e - \phi_o) - \cos(g_e[t]) \cos(\phi_e) \sin(\phi_e - \phi_o)) \\ & + 4 \cos(g_e[t]) \cos^2(\theta_e) \times \sin(\phi_e) (\cos^2(\theta_o) \cos(\phi_o) \cos(\phi_e - \phi_o) - \sin(\phi_o) \sin(\phi_e - \phi_o)) \\ & + \sin(g_e[t]) \cos(\theta_e) (-2 \sin^2(\theta_o) \cos(2\phi_o) + \cos(2\theta_o) + 3) - 4 \sin(\phi_o) (\cos(g_e[t]) \cos(\phi_e) \cos(\phi_e - \phi_o) \\ & + \sin^2(\theta_e) \sin(\phi_e) \sin(\phi_e - \phi_o))] + 8 \sin^2(\theta_e) \sin(\phi_e) \sin^2(\theta_o) \cos(\phi_o) \times (\cos(\phi_e - \phi_o) - \cos(g_e[t]) \cos(\phi_e) \cos(\phi_o)) \\ & \left. - 8 \sin^2(\theta_e) \sin^2(\phi_e) \sin(g_o[t]) \cos(\theta_o) - 2 \cos(g_e[t]) \sin(g_o[t]) \cos(\theta_o) \times (2 \sin^2(\theta_e) \cos(2\phi_e) + \cos(2\theta_e) + 3) \right\}, \end{aligned}$$

$$\begin{aligned} \xi_{yz}(t) = & J \sin(\theta_o) \left\{ \cos(g_e[t]) \cos^2(\theta_e) \sin(\phi_e) \left(2 \sin^2\left(\frac{g_o[t]}{2}\right) \cos(\theta_o) \cos(\phi_e - \phi_o) + \sin(g_o[t]) \sin(\phi_e - \phi_o) \right) \right. \\ & + \sin(g_e[t]) \cos(\theta_e) \left(2 \sin^2\left(\frac{g_o[t]}{2}\right) \cos(\theta_o) \cos(\phi_o) - \sin(g_o[t]) \sin(\phi_o) \right) \\ & + \cos(\phi_e - \phi_o) \left(2 \sin^2(\theta_e) \sin(\phi_e) \sin^2\left(\frac{g_o[t]}{2}\right) \cos(\theta_o) + \cos(g_e[t]) \cos(\phi_e) \sin(g_o[t]) \right) \\ & \left. + \sin(\phi_e - \phi_o) \left(\sin^2(\theta_e) \sin(\phi_e) \sin(g_o[t]) - 2 \cos(g_e[t]) \cos(\phi_e) \sin^2\left(\frac{g_o[t]}{2}\right) \cos(\theta_o) \right) \right\}, \end{aligned}$$

$$\begin{aligned} \xi_{zy}(t) = & J \sin(\theta_e) \{ \cos(g_o[t]) [\sin(g_e[t]) \cos(\phi_e) (\cos^2(\theta_o) \sin^2(\phi_o) + \cos^2(\phi_o)) - (\cos(g_e[t]) - 1) \cos(\theta_e) [\cos^2(\theta_o) \sin(\phi_o) \\ & \times \cos(\phi_e - \phi_o) + \cos(\phi_o) \sin(\phi_e - \phi_o)] + \sin(g_e[t]) \sin(\phi_e) \sin^2(\theta_o) \sin(\phi_o) \cos(\phi_o)] - \sin^2(\theta_o) \sin(\phi_o) \\ & \times [(\cos(g_e[t]) - 1) \cos(\theta_e) \cos(\phi_e - \phi_o) + \sin(g_e[t]) \sin(\phi_e - \phi_o)] - \sin(g_o[t]) \cos(\theta_o) [(\cos(g_e[t]) - 1) \cos(\theta_e) \cos(\phi_e) \\ & + \sin(g_e[t]) \sin(\phi_e)] \}, \end{aligned}$$

$$\begin{aligned} \xi_{zx}(t) = & J \sin(\theta_o) \left\{ \cos(g_e[t]) \left[\cos(\phi_e - \phi_o) \left(2 \cos^2(\theta_e) \cos(\phi_e) \sin^2\left(\frac{g_o[t]}{2}\right) \cos(\theta_o) - \sin(\phi_e) \sin(g_o[t]) \right) \right. \right. \\ & \left. + \sin(\phi_e - \phi_o) \times \left(2 \sin(\phi_e) \sin^2\left(\frac{g_o[t]}{2}\right) \cos(\theta_o) + \cos^2(\theta_e) \cos(\phi_e) \sin(g_o[t]) \right) \right] \\ & + \sin^2(\theta_e) \cos(\phi_e) \left(2 \sin^2\left(\frac{g_o[t]}{2}\right) \cos(\theta_o) \cos(\phi_e - \phi_o) + \sin(g_o[t]) \sin(\phi_e - \phi_o) \right) \\ & \left. - \sin(g_e[t]) \cos(\theta_e) \left(2 \sin^2\left(\frac{g_o[t]}{2}\right) \cos(\theta_o) \sin(\phi_o) + \sin(g_o[t]) \cos(\phi_o) \right) \right\}, \end{aligned}$$

$$\begin{aligned} \xi_{xz}(t) = & J \sin(\theta_e) \left\{ \sin^2(\theta_o) \cos(\phi_o) \left[2 \sin^2\left(\frac{g_e[t]}{2}\right) \cos(\theta_e) \cos(\phi_e - \phi_o) - \sin(g_e[t]) \sin(\phi_e - \phi_o) \right] - \cos(g_o[t]) [\sin(g_e[t]) \right. \\ & \times (\cos^2(\theta_o) \cos(\phi_o) \sin(\phi_e - \phi_o) + \sin(\phi_o) \cos(\phi_e - \phi_o)) + (\cos(g_e[t]) - 1) \cos(\theta_e) (\cos^2(\theta_o) \cos(\phi_o) \cos(\phi_e - \phi_o) \\ & \left. - \sin(\phi_o) \sin(\phi_e - \phi_o))] - \sin(g_o[t]) \cos(\theta_o) [\sin(g_e[t]) \cos(\phi_e) - (\cos(g_e[t]) - 1) \cos(\theta_e) \sin(\phi_e)] \right\}, \end{aligned}$$

where we state explicitly the time dependence of even and odd integral terms $g_e[t]$ and $g_o[t]$, respectively.

Once we have rotated the Hamiltonian into a suitable frame, the corresponding unitary operator for the evolution during a period T can be rewritten using the Magnus expansion [41]:

$$\hat{\mathcal{U}}(T) = \hat{T} \exp\left(-i \int_0^T dt' \hat{\mathcal{H}}'(t')\right) \approx \exp(-i \hat{\mathcal{H}}_F T), \quad (\text{A9})$$

with the Floquet Hamiltonian $\hat{\mathcal{H}}_F = \hat{\mathcal{H}}_F^{(0)} + \hat{\mathcal{H}}_F^{(1)} + \hat{\mathcal{H}}_F^{(2)} + \dots$, which consists of corrections in $\mathcal{O}[1/\omega]$. They can be written as

$$\hat{\mathcal{H}}_F^{(0)} = \frac{1}{T} \int_0^T dt' \hat{\mathcal{H}}'(t'), \quad (\text{A10})$$

$$\hat{\mathcal{H}}_F^{(1)} = \frac{-i}{2!T} \int_0^T dt' \int_0^{t'} dt'' [\hat{\mathcal{H}}'(t'), \hat{\mathcal{H}}'(t'')], \quad (\text{A11})$$

$$\begin{aligned} \hat{\mathcal{H}}_F^{(2)} = & \frac{1}{3!T} \int_0^T dt' \int_0^{t'} dt'' \int_0^{t''} dt''' \{ [\hat{\mathcal{H}}'(t'), \hat{\mathcal{H}}'(t'')], \hat{\mathcal{H}}'(t''') \} \\ & + [[\hat{\mathcal{H}}'(t'''), \hat{\mathcal{H}}'(t'')], \hat{\mathcal{H}}'(t') \} \}, \end{aligned} \quad (\text{A12})$$

and higher-order terms can be written in a similar way using nested commutators. We notice that $\|\hat{\mathcal{H}}_F^{(k)}\| \sim (1/\omega)^k$, and thus for very small time intervals, given by the period of the oscillating term $T = 2\pi/\omega \rightarrow 0$ (infinite-frequency limit), the effective Floquet Hamiltonian is represented by the period average of the time-dependent

Hamiltonian written in Eq. (A10). In this work, we consider the Floquet Hamiltonian only to the lowest order, $\hat{\mathcal{H}}_F = \hat{\mathcal{H}}_F^{(0)}$, while higher-order corrections $\sim (1/\omega)^k$ ($k > 0$) are accounted for in the numerical integration of the full time-dependent Hamiltonian.

Finally, let us choose the form of the oscillatory magnetic field and find the period-averaged Floquet Hamiltonian for the transmon chain. This can be chosen in the form

$$f_{e/o}(t) = \frac{\lambda_{e/o}\omega}{2h_{e/o}} \cos(\omega t + \varphi_{e/o}), \quad (\text{A13})$$

where $\lambda_{e/o}$ are constants of order unity and $\varphi_{e/o}$ are initial phases for the modulation. The latter is of high importance in the Floquet formalism, as it leads to kick-operator terms which change the basis of the system but do not enter the effective time-independent Hamiltonian [43]. However, in the current study we are interested in actual protocols with Floquet simulation, where the drive term is abruptly turned on at time point $t_0 = 0$, and the initial phase of the drive may be important. Here we consider zero initial phases $\varphi_{e/o} = 0$, such that the kick operator is unity.

The integral functions $g_{e/o}[t]$ are given by

$$g_{e/o}[t] = \lambda_{e/o} \sin(\omega t). \quad (\text{A14})$$

Then, the period-averaged coefficients $\overline{\xi_{\alpha\alpha'}} = (1/2\pi) \int_0^{2\pi} d\tau \xi_{\alpha\alpha'}(\tau)$ can be written in the form

$$\begin{aligned} \overline{\xi_{xx}} = & J[\sin^2(\theta_e) \cos(\phi_e) \mathcal{J}_0(\lambda_o)(\cos^2(\theta_o) \cos(\phi_o) \cos(\phi_e - \phi_o) - \sin(\phi_o) \sin(\phi_e - \phi_o)) \\ & + \sin^2(\theta_o) \cos(\phi_o) [\mathcal{J}_0(\lambda_e)(\cos^2(\theta_e) \cos(\phi_e) \cos(\phi_e - \phi_o) + \sin(\phi_e) \sin(\phi_e - \phi_o)) + \sin^2(\theta_e) \cos(\phi_e) \cos(\phi_e - \phi_o)] \\ & + \frac{\mathcal{J}_0(\lambda_e + \lambda_o)}{2} [\cos^2(\theta_e) \cos(\phi_e) (\cos^2(\theta_o) \cos(\phi_o) \cos(\phi_e - \phi_o) - \sin(\phi_o) \sin(\phi_e - \phi_o)) \\ & + \sin(\phi_e) (\cos^2(\theta_o) \cos(\phi_o) \sin(\phi_e - \phi_o) + \sin(\phi_o) \cos(\phi_e - \phi_o)) - \cos(\theta_e) \cos(\theta_o)] \\ & + \frac{\mathcal{J}_0(\lambda_e - \lambda_o)}{2} [\cos^2(\theta_e) \cos(\phi_e) (\cos^2(\theta_o) \cos(\phi_o) \cos(\phi_e - \phi_o) - \sin(\phi_o) \sin(\phi_e - \phi_o)) \\ & + \sin(\phi_e) (\cos^2(\theta_o) \cos(\phi_o) \sin(\phi_e - \phi_o) + \sin(\phi_o) \cos(\phi_e - \phi_o)) + \cos(\theta_e) \cos(\theta_o)], \end{aligned}$$

$$\begin{aligned} \overline{\xi_{yy}} = & J\{\sin^2(\theta_e) \sin(\phi_e) \mathcal{J}_0(\lambda_o)(\cos^2(\theta_o) \sin(\phi_o) \cos(\phi_e - \phi_o) + \cos(\phi_o) \sin(\phi_e - \phi_o)) \\ & + \sin^2(\theta_o) \sin(\phi_o) [\sin(\phi_e) \cos(\phi_e - \phi_o) (\cos^2(\theta_e) \mathcal{J}_0(\lambda_e) + \sin^2(\theta_e)) - \mathcal{J}_0(\lambda_e) \cos(\phi_e) \sin(\phi_e - \phi_o)]\} \\ & + \frac{\mathcal{J}_0(\lambda_e + \lambda_o)}{2} \{\cos(\phi_e) [\cos(\phi_e) (\cos^2(\theta_o) \sin^2(\phi_o) + \cos^2(\phi_o)) + \sin(\phi_e) \sin^2(\theta_o) \sin(\phi_o) \cos(\phi_o)] \\ & + \cos^2(\theta_e) \sin(\phi_e) (\cos^2(\theta_o) \sin(\phi_o) \cos(\phi_e - \phi_o) + \cos(\phi_o) \sin(\phi_e - \phi_o)) - \cos(\theta_e) \cos(\theta_o)\} \\ & + \frac{\mathcal{J}_0(\lambda_e - \lambda_o)}{2} \{\cos(\phi_e) [\cos(\phi_e) (\cos^2(\theta_o) \sin^2(\phi_o) + \cos^2(\phi_o)) + \sin(\phi_e) \sin^2(\theta_o) \sin(\phi_o) \cos(\phi_o)] \\ & + \cos^2(\theta_e) \sin(\phi_e) (\cos^2(\theta_o) \sin(\phi_o) \cos(\phi_e - \phi_o) + \cos(\phi_o) \sin(\phi_e - \phi_o)) + \cos(\theta_e) \cos(\theta_o)\}, \end{aligned}$$

$$\overline{\xi_{zz}} = J \frac{1}{2} \sin(\theta_e) \sin(\theta_o) \cos(\phi_e - \phi_o) \{ 2 \cos(\theta_e) \cos(\theta_o) (1 - \mathcal{J}_0(\lambda_e) - \mathcal{J}_0(\lambda_o)) + (\cos(\theta_e) \cos(\theta_o) - 1) \mathcal{J}_0(\lambda_e + \lambda_o) + (\cos(\theta_e) \cos(\theta_o) + 1) \mathcal{J}_0(\lambda_e - \lambda_o) \},$$

$$\overline{\xi_{xy}} = J \frac{1}{16} \{ \sin^2(\theta_o) \sin(2\phi_o) [2 \sin^2(\theta_e) [2 - 4 \cos^2(\phi_e) \mathcal{J}_0(\lambda_o) + \cos(2\phi_e) (\mathcal{J}_0(\lambda_e - \lambda_o) + \mathcal{J}_0(\lambda_e + \lambda_o) - 2 \mathcal{J}_0(\lambda_e) + 2)] + (\cos(2\theta_e) + 3) (2 \mathcal{J}_0(\lambda_e) - \mathcal{J}_0(\lambda_e - \lambda_o) - \mathcal{J}_0(\lambda_e + \lambda_o))] + \sin^2(\theta_e) \sin(2\phi_e) [(2 \mathcal{J}_0(\lambda_o) - \mathcal{J}_0(\lambda_e - \lambda_o) - \mathcal{J}_0(\lambda_e + \lambda_o)) (2 \sin^2(\theta_o) \cos(2\phi_o) + \cos(2\theta_o) + 3) - 8 (\mathcal{J}_0(\lambda_e) - 1) \sin^2(\theta_o) \sin^2(\phi_o)] \},$$

$$\overline{\xi_{yx}} = J \frac{1}{2} \{ \sin^2(\theta_e) [(1 - \mathcal{J}_0(\lambda_e)) \sin(2\phi_e) \sin^2(\theta_o) \cos^2(\phi_o) + 2 \sin(\phi_e) \mathcal{J}_0(\lambda_o) (\cos^2(\theta_o) \cos(\phi_o) \cos(\phi_e - \phi_o) - \sin(\phi_o) \sin(\phi_e - \phi_o))] + \sin^2(\theta_o) \sin(2\phi_o) [\sin^2(\phi_e) (\cos^2(\theta_e) \mathcal{J}_0(\lambda_e) + \sin^2(\theta_e)) + \mathcal{J}_0(\lambda_e) \cos^2(\phi_e)] + \mathcal{J}_0(\lambda_e - \lambda_o) [\cos^2(\theta_e) \sin(\phi_e) (\cos^2(\theta_o) \cos(\phi_o) \cos(\phi_e - \phi_o) - \sin(\phi_o) \sin(\phi_e - \phi_o)) - \cos(\phi_e) (\cos^2(\theta_o) \cos(\phi_o) \sin(\phi_e - \phi_o) + \sin(\phi_o) \cos(\phi_e - \phi_o))] + \mathcal{J}_0(\lambda_e + \lambda_o) [\cos^2(\theta_e) \sin(\phi_e) (\cos^2(\theta_o) \cos(\phi_o) \cos(\phi_e - \phi_o) - \sin(\phi_o) \sin(\phi_e - \phi_o)) - \cos(\phi_e) (\cos^2(\theta_o) \cos(\phi_o) \sin(\phi_e - \phi_o) + \sin(\phi_o) \cos(\phi_e - \phi_o))] \},$$

$$\overline{\xi_{yz}} = J \frac{1}{2} \{ \sin(2\theta_o) [\sin(\phi_e) \cos(\phi_e - \phi_o) [\cos^2(\theta_e) \mathcal{J}_0(\lambda_e) - \sin^2(\theta_e) (\mathcal{J}_0(\lambda_o) - 1)] - \mathcal{J}_0(\lambda_e) \cos(\phi_e) \sin(\phi_e - \phi_o)] - \sin(\theta_o) \mathcal{J}_0(\lambda_e - \lambda_o) (\cos^2(\theta_e) \sin(\phi_e) \cos(\theta_o) \cos(\phi_e - \phi_o) + \cos(\theta_e) \sin(\phi_o) - \cos(\phi_e) \cos(\theta_o) \sin(\phi_e - \phi_o)) + \sin(\theta_o) \mathcal{J}_0(\lambda_e + \lambda_o) [\cos(\theta_e) \sin(\phi_o) + \cos(\phi_e) \cos(\theta_o) \sin(\phi_e - \phi_o) - \cos^2(\theta_e) \sin(\phi_e) \cos(\theta_o) \cos(\phi_e - \phi_o)] \},$$

$$\overline{\xi_{zy}} = J \frac{1}{2} \sin(\theta_e) \{ -\cos(\theta_e) (\mathcal{J}_0(\lambda_e - \lambda_o) + \mathcal{J}_0(\lambda_e + \lambda_o) - 2 \mathcal{J}_0(\lambda_o)) (\cos^2(\theta_o) \sin(\phi_o) \cos(\phi_e - \phi_o) + \cos(\phi_o) \sin(\phi_e - \phi_o)) - 2 \cos(\theta_e) (\mathcal{J}_0(\lambda_e) - 1) \sin^2(\theta_o) \sin(\phi_o) \cos(\phi_e - \phi_o) + \sin(\phi_e) \cos(\theta_o) (\mathcal{J}_0(\lambda_e + \lambda_o) - \mathcal{J}_0(\lambda_e - \lambda_o)) \},$$

$$\overline{\xi_{xz}} = J \frac{1}{2} \{ \sin(2\theta_o) [\cos(\phi_e) \cos(\phi_e - \phi_o) [\cos^2(\theta_e) \mathcal{J}_0(\lambda_e) - \sin^2(\theta_e) (\mathcal{J}_0(\lambda_o) - 1)] + \mathcal{J}_0(\lambda_e) \sin(\phi_e) \sin(\phi_e - \phi_o)] - \sin(\theta_o) \mathcal{J}_0(\lambda_e + \lambda_o) (\cos^2(\theta_e) \cos(\phi_e) \cos(\theta_o) \cos(\phi_e - \phi_o) - \cos(\theta_e) \cos(\phi_o) + \sin(\phi_e) \cos(\theta_o) \sin(\phi_e - \phi_o)) - \sin(\theta_o) \mathcal{J}_0(\lambda_e - \lambda_o) [\cos(\theta_e) (\cos(\theta_e) \cos(\phi_e) \cos(\theta_o) \cos(\phi_e - \phi_o) + \cos(\phi_o)) + \sin(\phi_e) \cos(\theta_o) \sin(\phi_e - \phi_o)] \},$$

$$\overline{\xi_{zx}} = J \frac{1}{2} \{ \sin(2\theta_e) [\cos(\phi_o) \cos(\phi_e - \phi_o) [\cos^2(\theta_o) \mathcal{J}_0(\lambda_o) - (\mathcal{J}_0(\lambda_e) - 1) \sin^2(\theta_o)] - \mathcal{J}_0(\lambda_o) \sin(\phi_o) \sin(\phi_e - \phi_o)] + \sin(\theta_e) \mathcal{J}_0(\lambda_e + \lambda_o) (\cos(\phi_e) \cos(\theta_o) + \cos(\theta_e) \sin(\phi_o) \sin(\phi_e - \phi_o) - \cos(\theta_e) \cos^2(\theta_o) \cos(\phi_o) \cos(\phi_e - \phi_o)) - \sin(\theta_e) \mathcal{J}_0(\lambda_e - \lambda_o) [\cos(\theta_o) (\cos(\theta_e) \cos(\theta_o) \cos(\phi_o) \cos(\phi_e - \phi_o) + \cos(\phi_e)) - \cos(\theta_e) \sin(\phi_o) \sin(\phi_e - \phi_o)] \}.$$

The above equations define the exact form of the generic Hamiltonian (4) from the main text and, thus, describe the possible Hamiltonians accessible for the Floquet quantum simulation with this method, assuming different even or odd periodic cosine modulation.

APPENDIX B: TRANSVERSE ISING MODEL DERIVATION

In this Appendix, we provide a procedure to engineer the transverse Ising Hamiltonian as an effective Floquet Hamiltonian of the isotropic XY model with transverse and longitudinal fields. For this, we consider a system with two (odd and even) sublattices, where only one of the

sublattices experiences fast oscillations of the magnetic field (see the sketch in Fig. 9).

Taking the full solution from Appendix A, the starting Hamiltonian for the simulation of the Ising model in the transmon chain reads

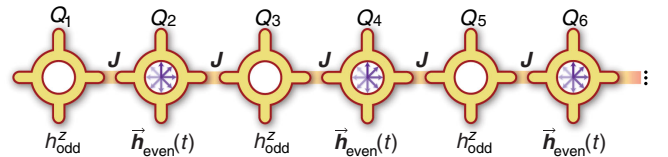


FIG. 9. Superconducting qubit chain with isotropic XY interaction J , a static effective magnetic field in the z direction on the odd sublattice, h_{odd}^z , and a fast time-dependent magnetic field acting on even sublattice sites, $\mathbf{h}_{\text{even}}(t)$.

$$\hat{\mathcal{H}}(t) = J \sum_{j=1}^{N-1} (\sigma_j^x \sigma_{j+1}^x + \sigma_j^y \sigma_{j+1}^y) + \sum_{j=1}^{\lfloor N/2 \rfloor} \frac{\lambda}{2} \omega \cos(\omega t) \sigma_{2j}^x + \hat{\mathcal{H}}_{\text{magn}}(t), \quad (\text{B1})$$

where $\lambda (\equiv \lambda_{\text{even}})$ is a drive parameter and $\mathcal{J}_0[x]$ denotes the zeroth-order Bessel function of the first kind. In the infinite-frequency limit $|J|/\omega \rightarrow 0$ and for $\lambda = 2.40483$ (such that $\mathcal{J}_0[\lambda] = 0$), the interaction term can be reduced to the Ising type. Additionally, the last term in Eq. (B1) is designed to introduce a transverse effective magnetic field and can be written as

$$\hat{\mathcal{H}}_{\text{magn}}(t) = \sum_{j=1}^{\lfloor N/2 \rfloor} h^z \sigma_{2j-1}^z + \frac{2h^z}{1 + \mathcal{J}_0[2\lambda]} \sum_{j=1}^{\lfloor N/2 \rfloor} \cos(\lambda \sin[\omega t]) \sigma_{2j}^z. \quad (\text{B2})$$

The first term in Eq. (B2) is a static magnetic field on the odd sublattice and commutes trivially with the fast oscillation part. However, the magnetic field on the even sublattice can be modified by the drive. The second term representing the magnetic field deviates from the general form considered in Appendix A, since it does not have the same time dependence. As opposed to the other field, however, the magnitude of this field does not increase with increasing ω and can thus be treated as a perturbation in the limit of large ω . Since it does not commute with the main driving field, it will be strongly modified by the drive. Going to the rotating frame with the unitary operator $\hat{U}_R(t) = \exp\{i\lambda \sin(\omega t)\}$, the magnetic term becomes

$$\hat{\mathcal{H}}'_{\text{magn}}(t) = h^z \sum_{j=1}^{\lfloor N/2 \rfloor} \sigma_{2j-1}^z + \frac{2h^z}{1 + \mathcal{J}_0[2\lambda]} \cos(\lambda \sin[\omega t]) \times \sum_{j=1}^{\lfloor N/2 \rfloor} \{\cos[\lambda \sin(\omega t)] \sigma_{2j}^z + \sin[\lambda \sin(\omega t)] \sigma_{2j}^y\}. \quad (\text{B3})$$

Finally, performing the period averaging, the σ_{2j}^y term vanishes, since the sine function oscillates between positive and negative values. At the same time, given that λ is fixed by the condition $\mathcal{J}_0[\lambda] = 0$, the integral $\int_0^{2\pi} dx \cos^2(\lambda \sin[x]) = \pi(1 + \mathcal{J}_0[2\lambda])$ gives a finite result:

$$\hat{\mathcal{H}}_F^{\text{magn}} = h^z \sum_{j=1}^N \sigma_j^z, \quad (\text{B4})$$

thus allowing us to introduce an effective transverse field h^z .

APPENDIX C: DIGITAL SIMULATION OF TRANSVERSE ISING MODEL

In this Appendix, we describe the digital simulation protocol, which we use to benchmark the performance of the Floquet quantum simulator. The transverse Ising model simulation, which we consider, is theoretically described in Ref. [17] and experimentally realized in Ref. [18]. The circuit scheme is shown in Fig. 10.

The algorithm relies on the realization of a unitary transformation with the effective Hamiltonian of interest using repetitions of a small step, corresponding to the Trotterization procedure. The protocol for the simulation of an arbitrary m -local Hamiltonian $\hat{\mathcal{H}}$ (generally not available in the physical setup) relies on the sequential implementation of the available parts of a Hamiltonian $\hat{\mathcal{H}}_k$ (constructed from gates acting on m qubits) such that $\sum_k \hat{\mathcal{H}}_k = \hat{\mathcal{H}}$. The corresponding unitary of a single digital step j of duration δt reads

$$\hat{U}_j(\delta t) = e^{-i\hat{\mathcal{H}}_1 \delta t} e^{-i\hat{\mathcal{H}}_2 \delta t} \dots e^{-i\hat{\mathcal{H}}_k \delta t}, \quad (\text{C1})$$

and the implementation of $N_{\text{Tr}} \rightarrow \infty$ Trotter steps combines into the unitary $\hat{U}(t) = \lim_{N_{\text{Tr}} \rightarrow \infty} \hat{U}_j(\delta t)^{N_{\text{Tr}}} \approx e^{-i\hat{\mathcal{H}}t}$.

In this spirit, the implementation of the transverse Ising model is proposed to rely on multiple applications of the Trotter step graphically shown in Fig. 10. It starts with the implementation of $U_{XY} = \exp\{-i\delta t \sum_{j=1}^{N/2} \hat{\mathcal{H}}_{2j-1,2j}^{(+)}\}$,

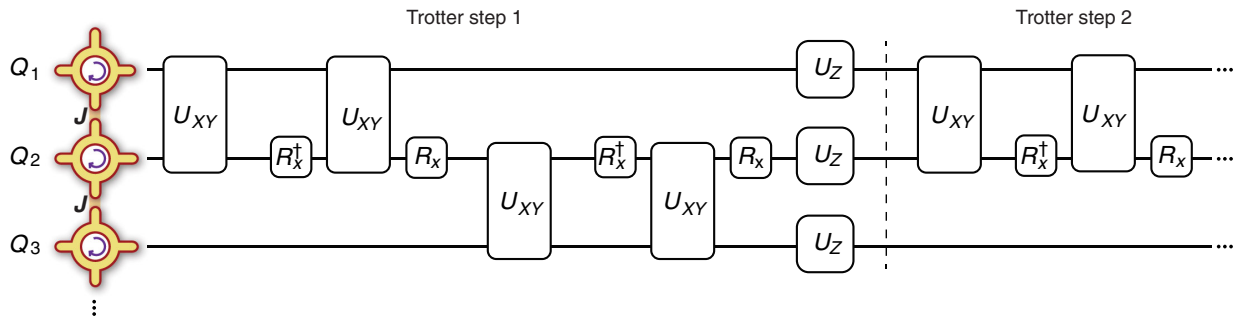


FIG. 10. Digital simulation scheme from Ref. [17]. It relies on Trotterization of the isotropic XY model dynamics, where additional single-qubit rotations at every second site effectively eliminate the YY coupling.

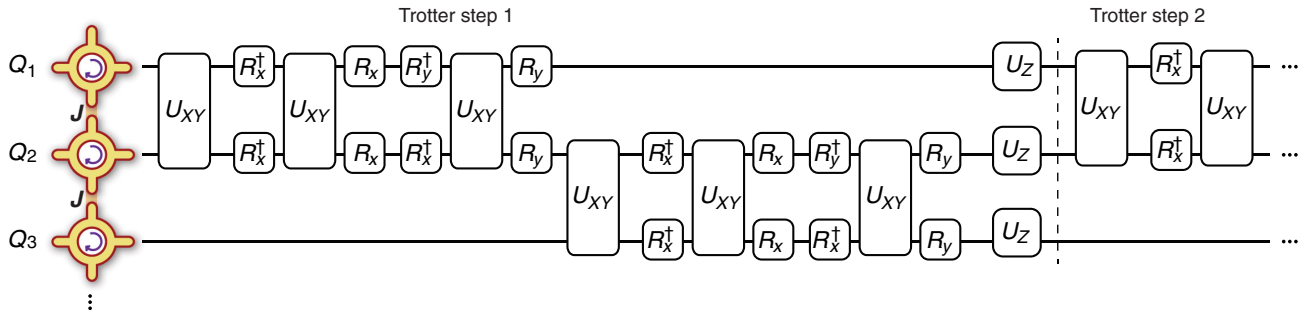


FIG. 11. Digital simulation scheme of the Heisenberg-type model from Ref. [17]. It relies on the sequential application of bare XY couplings [$\propto \alpha_{xy}J(\sigma_j^x\sigma_{j+1}^x + \sigma_j^y\sigma_{j+1}^y)$] and its $\pi/2$ rotated version corresponding to XZ [$\propto \alpha_{xz}J(\sigma_j^x\sigma_{j+1}^x + \sigma_j^z\sigma_{j+1}^z)$] and YZ [$\propto \alpha_{yz}J(\sigma_j^y\sigma_{j+1}^y + \sigma_j^z\sigma_{j+1}^z)$] interactions. Here $\alpha_{xy,xz,yz}$ correspond to dimensionless coefficients which allow tuning the model into the anisotropic XYZ model. We note that the described sequence can be further optimized by combing single-qubit rotations to unity matrices and z rotations. Moreover, the ordering of the terms can be changed to optimize the procedure.

where by $\hat{H}_{j,j'}^{(+)} = (J/2)(\sigma_j^x\sigma_{j'}^x + \sigma_j^y\sigma_{j'}^y)$ we define the simple application of XY interaction for each pair of qubits. Next, this unitary can be rotated by applying π rotations around x axis for every second qubit, $\hat{R}_x = \exp\{-i(\pi/2)\sum_{j=1}^{N/2}\sigma_{2j}^x\}$, which leads to $\hat{R}_x^\dagger U_{XY} \hat{R}_x = \exp\{-i\delta t \sum_{j=1}^{N/2} \hat{H}_{2j-1,2j}^{(-)}\}$, where we define $\hat{H}_{j,j'}^{(-)} = (J/2)(\sigma_j^x\sigma_{j'}^x - \sigma_j^y\sigma_{j'}^y)$ as the XY Hamiltonian with the YY term flipped by rotation. Finally, the last layer in the Trotter step implements the transverse fields with $U_Z = \exp\{-i\delta t h^z \sum_{j=1}^N \sigma_j^z\}$. Once the Trotter step is repeated many times, the noncommuting Hamiltonian parts can be added, thus implementing the transverse Ising model digitally.

The same considerations can be repeated for the digitized annealing procedure [19]. Here the important part is to keep the phase applied by the U_Z gates consistent with the adiabatic evolution.

APPENDIX D: DIGITAL SIMULATION OF XYZ MODEL

The considered digital simulation protocol for the XYZ model, originally described in Ref. [17], is sketched in Fig. 11. It relies on the sequential rotation of the basis for nearest-neighbor interaction, such that in the limit of a large number of Trotter steps it sums up to $\sum_{j=1}^{N-1} (J^x \sigma_j^x \sigma_{j+1}^x + J^y \sigma_j^y \sigma_{j+1}^y + J^z \sigma_j^z \sigma_{j+1}^z)$. First, the XY unitary is performed, implementing $U_{XY} = \exp\{-i\delta t \sum_{j=1}^{N-1} \alpha_{xy} J(\sigma_j^x \sigma_{j+1}^x + \sigma_j^y \sigma_{j+1}^y)\}$, where α_{xy} is some constant. Next, applying $\pi/2$ rotation around the x axis for each qubit, $\hat{R}_x = \exp\{-i(\pi/4)\sum_{j=1}^N \sigma_j^x\}$, the two-qubit unitary can be transformed to $U_{XZ} = \exp\{-i\delta t \sum_{j=1}^{N-1} \alpha_{xz} J(\sigma_j^x \sigma_{j+1}^x + \sigma_j^z \sigma_{j+1}^z)\}$. Subsequent $\pi/2$ rotation around the y axis implements the $U_{YZ} = \exp\{-i\delta t \sum_{j=1}^{N/2} \alpha_{yz} J(\sigma_j^y \sigma_{j+1}^y + \sigma_j^z \sigma_{j+1}^z)\}$ interaction. For instance, the final chosen

configuration of $J_y = 2J^x/3$, $J^z = J^x/3$ can be achieved by choosing $J_x = J$ (can be different from J_{sim}), $\alpha_{xy} = 2/3$, $\alpha_{xz} = 1/3$, and $\alpha_{yz} = 0$, simplifying the gate sequence. Finally, the U_Z operation introduces an effective magnetic field in the z direction which allows for annealing to the ground state of the XYZ model. The linear schedule can then be designed similarly to the nonstoquastic case considered in Ref. [19]. While the sequence represented in Fig. 11 works perfectly in the $N_{\text{Tr}} \rightarrow \infty$ limit, we note that the order of the unitaries $\{\mathcal{S}\} = \{U_{XY}, U_{XZ}, U_{YZ}, U_Z\}$, which form a Trotter step, alter the final infidelity for the annealed state. Thus, for the digital simulation procedure, we consider 24 permutations of unitaries for the set \mathcal{S} and choose the sequence of the step which yields minimal infidelity.

We note that alternatively the XYZ model can be simulated with controlled-phase (ZZ) gates as described by Barends *et al.* [19].

- [1] S. Lloyd, Universal quantum simulators, *Science* **273**, 1073 (1996).
- [2] D. Wecker, M. B. Hastings, N. Wiebe, B. K. Clark, C. Nayak, and M. Troyer, Solving strongly correlated electron models on a quantum computer, *Phys. Rev. A* **92**, 062318 (2015).
- [3] D. Wecker, B. Bauer, B. K. Clark, M. B. Hastings, and M. Troyer, Gate-count estimates for performing quantum chemistry on small quantum computers, *Phys. Rev. A* **90**, 022305 (2014).
- [4] M. Reiher, N. Wiebe, K. M. Svore, D. Wecker, and M. Troyer, Elucidating reaction mechanisms on quantum computers, *Proc. Natl. Acad. Sci. U.S.A.* **114**, 7555 (2017).
- [5] M. A. Nielsen and I. L. Chuang, *Quantum Computation and Quantum Information* (Cambridge University Press, Cambridge, England, 2010).
- [6] I. M. Georgescu, S. Ashhab, and Franco Nori, Quantum simulation, *Rev. Mod. Phys.* **86**, 153 (2014).

- [7] A. Wallraff, D. I. Schuster, A. Blais, L. Frunzio, R.-S. Huang, J. Majer, S. Kumar, S. M. Girvin, and R. J. Schoelkopf, Circuit quantum electrodynamics: Coherent coupling of a single photon to a Cooper pair box, *Nature (London)* **431**, 162 (2004).
- [8] M. H. Devoret and R. J. Schoelkopf, Superconducting circuits for quantum information: An outlook, *Science* **339**, 1169 (2013).
- [9] R. Barends, J. Kelly, A. Megrant, A. Veitia, D. Sank, E. Jeffrey, T. C. White, J. Mutus, A. G. Fowler, B. Campbell, Y. Chen, Z. Chen, B. Chiaro, A. Dunsworth, C. Neill, P. O'Malley, P. Roushan, A. Vainsencher, J. Wenner, A. N. Korotkov, A. N. Cleland, and J. M. Martinis, Superconducting quantum circuits at the surface code threshold for fault tolerance, *Nature (London)* **508**, 500 (2014).
- [10] J. Kelly, R. Barends, A. G. Fowler, A. Megrant, E. Jeffrey, T. C. White, D. Sank, J. Y. Mutus, B. Campbell, Yu Chen, Z. Chen, B. Chiaro, A. Dunsworth, I.-C. Hoi, C. Neill, P. J. J. O'Malley, C. Quintana, P. Roushan, A. Vainsencher, J. Wenner, A. N. Cleland, and John M. Martinis, State preservation by repetitive error detection in a superconducting quantum circuit, *Nature (London)* **519**, 66 (2015).
- [11] D. Risté, S. Poletto, M.-Z. Huang, A. Bruno, V. Vesterinen, O.-P. Saira, and L. DiCarlo, Detecting bit-flip errors in a logical qubit using stabilizer measurements, *Nat. Commun.* **6**, 6983 (2015).
- [12] A. D. Córcoles, E. Magesan, S. J. Srinivasan, A. W. Cross, M. Steffen, J. M. Gambetta, and J. M. Chow, Demonstration of a quantum error detection code using a square lattice of four superconducting qubits, *Nat. Commun.* **6**, 6979 (2015).
- [13] N. Ofek, A. Petrenko, R. Heeres, P. Reinhold, Z. Leghtas, B. Vlastakis, Y. Liu, L. Frunzio, S. M. Girvin, L. Jiang, M. Mirrahimi, M. H. Devoret, and R. J. Schoelkopf, Extending the lifetime of a quantum bit with error correction in superconducting circuits, *Nature (London)* **536**, 441 (2016).
- [14] M. D. Reed, L. DiCarlo, S. Nigg, L. Sun, L. Frunzio, S. M. Girvin, and R. J. Schoelkopf, Realization of three-qubit quantum error correction with superconducting circuits, *Nature (London)* **482**, 382 (2012).
- [15] J. H. Béjanin, T. G. McConkey, J. R. Rinehart, C. T. Earnest, C. R. H. McRae, D. Shiri, J. D. Bateman, Y. Rohanizadegan, B. Penava, P. Breul, S. Royak, M. Zapatka, A. G. Fowler, and M. Mariantoni, Three-Dimensional Wiring for Extensible Quantum Computing: The Quantum Socket, *Phys. Rev. Applied* **6**, 044010 (2016).
- [16] A. A. Houck, H. E. Türeci, and J. Koch, On-chip quantum simulation with superconducting circuits, *Nat. Phys.* **8**, 292 (2012).
- [17] U. Las Heras, A. Mezzacapo, L. Lamata, S. Filipp, A. Wallraff, and E. Solano, Digital Quantum Simulation of Spin Systems in Superconducting Circuits, *Phys. Rev. Lett.* **112**, 200501 (2014).
- [18] Y. Salathé, M. Mondal, M. Oppliger, J. Heinsoo, P. Kurpiers, A. Potočnik, A. Mezzacapo, U. Las Heras, L. Lamata, E. Solano, S. Filipp, and A. Wallraff, Digital Quantum Simulation of Spin Models with Circuit Quantum Electrodynamics, *Phys. Rev. X* **5**, 021027 (2015).
- [19] R. Barends *et al.*, Digitized adiabatic quantum computing with a superconducting circuit, *Nature (London)* **534**, 222 (2016).
- [20] R. Barends, L. Lamata, J. Kelly, L. Garca-Ivarez, A. G. Fowler, A. Megrant, E. Jeffrey, T. C. White, D. Sank, J. Y. Mutus, B. Campbell, Yu Chen, Z. Chen, B. Chiaro, A. Dunsworth, I.-C. Hoi, C. Neill, P. J. J. O'Malley, C. Quintana, P. Roushan, A. Vainsencher, J. Wenner, E. Solano, and J. M. Martinis, Digital quantum simulation of fermionic models with a superconducting circuit, *Nat. Commun.* **6**, 7654 (2015).
- [21] P. J. J. O'Malley *et al.*, Scalable Quantum Simulation of Molecular Energies, *Phys. Rev. X* **6**, 031007 (2016).
- [22] C. Neill, P. Roushan, M. Fang, Y. Chen, M. Kolodrubetz, Z. Chen, A. Megrant, R. Barends, B. Campbell, B. Chiaro, A. Dunsworth, E. Jeffrey, J. Kelly, J. Mutus, P. J. J. O'Malley, C. Quintana, D. Sank, A. Vainsencher, J. Wenner, T. C. White, A. Polkovnikov, and J. M. Martinis, Ergodic dynamics and thermalization in an isolated quantum system, *Nat. Phys.* **12**, 1037 (2016).
- [23] P. Roushan, C. Neill, A. Megrant, Y. Chen, R. Babbush, R. Barends, B. Campbell, Z. Chen, B. Chiaro, A. Dunsworth, A. Fowler, E. Jeffrey, J. Kelly, E. Lucero, J. Mutus, P. J. J. O'Malley, M. Neeley, C. Quintana, D. Sank, A. Vainsencher, J. Wenner, T. White, E. Kapit, H. Neven, and J. Martinis, Chiral ground-state currents of interacting photons in a synthetic magnetic field, *Nat. Phys.* **13**, 146 (2017).
- [24] D. Ballester, G. Romero, J. J. García-Ripoll, F. Deppe, and E. Solano, Quantum Simulation of the Ultrastrong-Coupling Dynamics in Circuit Quantum Electrodynamics, *Phys. Rev. X* **2**, 021007 (2012).
- [25] N. K. Langford, R. Sagastizabal, M. Kounalakis, C. Dickel, A. Bruno, F. Luthi, D. J. Thoen, A. Endo, and L. DiCarlo, Experimentally simulating the dynamics of quantum light and matter at ultrastrong coupling, *Nat. Commun.* **8**, 1715 (2017).
- [26] A. Mezzacapo, E. Rico, C. Sabn, I. L. Egusquiza, L. Lamata, and E. Solano, Non-Abelian SU(2) Lattice Gauge Theories in Superconducting Circuits, *Phys. Rev. Lett.* **115**, 240502 (2015).
- [27] I. Bloch, J. Dalibard, and S. Nascimbéne, Quantum simulations with ultracold quantum gases, *Nat. Phys.* **8**, 267 (2012).
- [28] J. Simon, W. S. Bakr, R. Ma, M. E. Tai, P. M. Preiss, and M. Greiner, Quantum simulation of antiferromagnetic spin chains in an optical lattice, *Nature (London)* **472**, 307 (2011).
- [29] K. Kim, M.-S. Chang, S. Korenblit, R. Islam, E. E. Edwards, J. K. Freericks, G.-D. Lin, L.-M. Duan, and C. Monroe, Quantum simulation of frustrated Ising spins with trapped ions, *Nature (London)* **465**, 590 (2010).
- [30] C. Senko, P. Richerme, J. Smith, A. Lee, I. Cohen, A. Retzker, and C. Monroe, Realization of a Quantum Integer-Spin Chain with Controllable Interactions, *Phys. Rev. X* **5**, 021026 (2015).
- [31] J. Zhang, G. Pagano, P. W. Hess, A. Kyprianidis, P. Becker, H. Kaplan, A. V. Gorshkov, Z.-X. Gong, and C. Monroe, Observation of a many-body dynamical phase transition with a 53-qubit quantum simulator, *Nature (London)* **551**, 601 (2017).

- [32] G. Wendin, Quantum information processing with superconducting circuits: A review, *Rep. Prog. Phys.* **80**, 106001 (2017).
- [33] L. Neumeier, M. Leib, and M. J. Hartmann, Single-Photon Transistor in Circuit Quantum Electrodynamics, *Phys. Rev. Lett.* **111**, 063601 (2013).
- [34] É. Dumur, B. Küng, A. K. Feofanov, T. Weissl, N. Roch, C. Naud, W. Guichard, and O. Buisson, V-shaped superconducting artificial atom based on two inductively coupled transmons, *Phys. Rev. B* **92**, 020515(R) (2015).
- [35] M. Sameti, A. Potocnik, D. E. Browne, A. Wallraff, and M. J. Hartmann, Superconducting quantum simulator for topological order and the toric code, *Phys. Rev. A* **95**, 042330 (2017).
- [36] Y. P. Zhong, D. Xu, P. Wang, C. Song, Q. J. Guo, W. X. Liu, K. Xu, B. X. Xia, C.-Y. Lu, Siyuan Han, Jian-Wei Pan, and H. Wang, Emulating Anyonic Fractional Statistical Behavior in a Superconducting Quantum Circuit, *Phys. Rev. Lett.* **117**, 110501 (2016).
- [37] Chao Song, Kai Xu, Wuxin Liu, Chuiping Yang, Shi-Biao Zheng, Hui Deng, Qiwei Xie, Keqiang Huang, Qiujiang Guo, Libo Zhang, Pengfei Zhang, Da Xu, Dongning Zheng, Xiaobo Zhu, H. Wang, Y.-A. Chen, C.-Y. Lu, Siyuan Han, and J.-W. Pan, 10-Qubit Entanglement and Parallel Logic Operations with a Superconducting Circuit, *Phys. Rev. Lett.* **119**, 180511 (2017).
- [38] P. Bertet, C. J. P. M. Harmans, and J. E. Mooij, Parametric coupling for superconducting qubits, *Phys. Rev. B* **73**, 064512 (2006).
- [39] A. Mezzacapo, L. Lamata, S. Filipp, and E. Solano, Many-Body Interactions with Tunable-Coupling Transmon Qubits, *Phys. Rev. Lett.* **113**, 050501 (2014).
- [40] E. Kapit, Universal two-qubit interactions, measurement, and cooling for quantum simulation and computing, *Phys. Rev. A* **92**, 012302 (2015).
- [41] M. Bukov, L. D'Alessio, and A. Polkovnikov, Universal high-frequency behavior of periodically driven systems: From dynamical stabilization to Floquet engineering, *Adv. Phys.* **64**, 139 (2015).
- [42] T. Iadecola, L. H. Santos, and C. Chamon, Stroboscopic symmetry-protected topological phases, *Phys. Rev. B* **92**, 125107 (2015).
- [43] N. Goldman and J. Dalibard, Periodically Driven Quantum Systems: Effective Hamiltonians and Engineered Gauge Fields, *Phys. Rev. X* **4**, 031027 (2014).
- [44] M. S. Rudner, N. H. Lindner, E. Berg, and M. Levin, Anomalous Edge States and the Bulk-Edge Correspondence for Periodically Driven Two-Dimensional Systems, *Phys. Rev. X* **3**, 031005 (2013).
- [45] L. Jiang, T. Kitagawa, J. Alicea, A. R. Akhmerov, D. Pekker, G. Refael, J. I. Cirac, E. Demler, M. D. Lukin, and P. Zoller, Majorana Fermions in Equilibrium and in Driven Cold-Atom Quantum Wires, *Phys. Rev. Lett.* **106**, 220402 (2011).
- [46] C. Deng, J.-L. Orgiazzi, F. Shen, S. Ashhab, and A. Lupascu, Observation of Floquet States in a Strongly Driven Artificial Atom, *Phys. Rev. Lett.* **115**, 133601 (2015).
- [47] Yu Chen, C. Neill, P. Roushan, N. Leung, M. Fang, R. Barends, J. Kelly, B. Campbell, Z. Chen, B. Chiaro, A. Dunsworth, E. Jeffrey, A. Megrant, J. Y. Mutus, P. J. J. O'Malley, C. M. Quintana, D. Sank, A. Vainsencher, J. Wenner, T. C. White, Michael R. Geller, A. N. Cleland, and J. M. Martinis, Qubit Architecture with High Coherence and Fast Tunable Coupling, *Phys. Rev. Lett.* **113**, 220502 (2014).
- [48] L. Casparis, T. W. Larsen, M. S. Olsen, F. Kuemmeth, P. Krogstrup, J. Nygård, K. D. Petersson, and C. M. Marcus, Gateon Benchmarking and Two-Qubit Operations, *Phys. Rev. Lett.* **116**, 150505 (2016).
- [49] R. Barends, J. Kelly, A. Megrant, D. Sank, E. Jeffrey, Y. Chen, Y. Yin, B. Chiaro, J. Mutus, C. Neill, P. O'Malley, P. Roushan, J. Wenner, T. C. White, A. N. Cleland, and John M. Martinis, Coherent Josephson Qubit Suitable for Scalable Quantum Integrated Circuits, *Phys. Rev. Lett.* **111**, 080502 (2013).
- [50] T. Kadowaki and H. Nishimori, Quantum annealing in the transverse Ising model, *Phys. Rev. E* **58**, 5355 (1998).
- [51] E. Farhi, J. Goldstone, S. Gutmann, and M. Sipser, Quantum computation by adiabatic evolution, [arXiv: quant-ph/0001106](https://arxiv.org/abs/quant-ph/0001106).
- [52] E. Farhi, J. Goldstone, S. Gutmann, J. Lapan, A. Lundgren, and D. Preda, A quantum adiabatic evolution algorithm applied to random instances of an NP-complete problem, *Science* **292**, 472 (2001).
- [53] M. A. Rol, C. C. Bultink, T. E. O'Brien, S. R. de Jong, L. S. Theis, X. Fu, F. Luthi, R. F. L. Vermeulen, J. C. de Sterke, A. Bruno, D. Deurloo, R. N. Schouten, F. K. Wilhelm, and L. DiCarlo, Restless Tuneup of High-Fidelity Qubit Gates, *Phys. Rev. Applied* **7**, 041001 (2017).
- [54] F. Motzoi, J. M. Gambetta, P. Rebentrost, and F. K. Wilhelm, Simple Pulses for Elimination of Leakage in Weakly Nonlinear Qubits, *Phys. Rev. Lett.* **103**, 110501 (2009).
- [55] J. M. Martinis and M. R. Geller, Fast adiabatic qubit gates using only σ_z control, *Phys. Rev. A* **90**, 022307 (2014).
- [56] S. André, L. Guo, V. Peano, M. Marthaler, and G. Schön, Emission spectrum of the driven nonlinear oscillator, *Phys. Rev. A* **85**, 053825 (2012).
- [57] J. M. Chow, J. M. Gambetta, A. D. Córcoles, S. T. Merkel, J. A. Smolin, C. Rigetti, S. Poletto, G. A. Keefe, M. B. Rothwell, J. R. Rozen, M. B. Ketchen, and M. Steffen, Universal Quantum Gate Set Approaching Fault-Tolerant Thresholds with Superconducting Qubits, *Phys. Rev. Lett.* **109**, 060501 (2012).
- [58] L. D'Alessio and M. Rigol, Long-time Behavior of Isolated Periodically Driven Interacting Lattice Systems, *Phys. Rev. X* **4**, 041048 (2014).
- [59] D. A. Abanin, W. De Roeck, and F. Huveneers, Exponentially Slow Heating in Periodically Driven Many-Body Systems, *Phys. Rev. Lett.* **115**, 256803 (2015).
- [60] T. Kuwahara, T. Mori, and K. Saito, Floquet-Magnus theory and generic transient dynamics in periodically driven many-body quantum systems, *Ann. Phys. (Amsterdam)* **367**, 96 (2016).
- [61] H. Nishimori and K. Takada, Exponential enhancement of the efficiency of quantum annealing by non-stochastic Hamiltonians, *Front. ICT* **4**, 2 (2017).